Journal of Computational Physics 508 (2024) 113014

Contents lists available at ScienceDirect

Journal of Computational Physics

journal homepage: www.elsevier.com/locate/jcp

The log-conformation formulation for single- and multi-phase axisymmetric viscoelastic flows

William Doherty [a,b], Timothy N. Phillips [b], Zhihua Xie [a,*]

[a] School of Engineering, Cardiff University, Queen's Buildings, Cardiff, CF24 3AA, UK
[b] School of Mathematics, Cardiff University, Abacws, Cardiff, CF24 4AG, UK

ARTICLE INFO

Keywords:
Multi-phase flow
Conservative level-set method
Axisymmetric
Viscoelastic fluid
Finite element method

ABSTRACT

A computational model for predicting axisymmetric single- and multi-phase viscoelastic flows based on the log-conformation formulation of the constitutive equation is presented. The governing equations are discretised using the finite element method and advanced in time using a projection scheme. The single-phase benchmark problem of viscoelastic flow past a sphere in a cylinder is considered and excellent agreement is found with the literature for the drag coefficient for an extensive range of Weissenberg numbers. The cause of the breakdown in stability due to a velocity inflection near the sphere is investigated. For multi-phase flows, enhanced stability of the conservative level-set method is obtained by introducing a diffused interface approach for normal calculations. This novel method is used to investigate the jump discontinuity phenomenon exhibited for a bubble rising in a viscoelastic fluid. Qualitative and quantitative agreement is found with contemporary literature in terms of the critical bubble volume as well as other phenomena such as the negative wake and trailing cusp.

Contents

1. Introduction . . . 2
2. Mathematical formulation . . . 3
   2.1. Governing equations . . . 3
   2.2. Log-conformation formulation . . . 4
   2.3. Conservative level-set method . . . 5
   2.4. Non-dimensional system . . . 6
3. Numerical discretisation . . . 7
   3.1. Spatial discretisation . . . 7
      3.1.1. Weak formulation of the governing equations . . . 7
      3.1.2. Weak formulation of the conservative level-set equations . . . 8
      3.1.3. SU/SUPG stabilisation method . . . 8
   3.2. Temporal discretisation . . . 8
4. Single-phase flow . . . 9
   4.1. Drag coefficient . . . 9
   4.2. Plots along paths . . . 11

* Corresponding author.
E-mail address: zxie@cardiff.ac.uk (Z. Xie).

https://doi.org/10.1016/j.jcp.2024.113014
Received 27 September 2023; Received in revised form 19 February 2024; Accepted 13 April 2024

Available online 17 April 2024

4.3. Contour plots . . . 13
5. Multi-phase flow . . . 13
5.1. Newtonian rising bubble . . . 15
5.2. Viscoelastic rising bubble . . . 15
5.2.1. Bubble metrics . . . 17
5.2.2. Negative wake . . . 18
5.2.3. Normal stress fields . . . 18
6. Conclusions . . . 19
CRediT authorship contribution statement . . . 20
Declaration of competing interest . . . 21
Data availability . . . 21
Acknowledgements . . . 21
Appendix A. Governing equations in cylindrical polar coordinates for axisymmetric viscoelastic flow . . . 21
References . . . 22

1. Introduction

Computational modelling of viscoelastic single- and multi-phase flows has applications in many contemporary research fields. A biological example of a single-phase flow is the flow of blood through narrow arteries. In the plastic manufacturing industry, the extrusion of polymer melts to create various products is an example of multi-phase flow that involves an interface between the molten polymer and surrounding air. The development of stable numerical schemes for simulating these flows is crucial when experiments involving viscoelastic fluids can be complex to construct [1,2].

Viscoelastic fluids differ from their traditional Newtonian counterparts in a number of significant ways [3]. They deform and flow like a Newtonian flow, but they also have the ability to exhibit memory dependent deformation and store/recover energy like an elastic solid. Thus the relationship between stress and strain is described by a non-linear rheological equation of state. The dimensionless group associated with elasticity is the Weissenberg number, Wi. For large values of Wi, many numerical schemes become unstable unless some form of stabilisation is implemented. The numerical instability is due to the inability of numerical schemes to capture the rapid changes in polymeric stress that can occur. This is known as the high Weissenberg number problem (HWNP) [4].

The study of single-phase axisymmetric viscoelastic flow encompasses a wide variety of physical and computational models. The benchmark problems in this field include axisymmetric contraction flow (see McKinley et al. [5]) and flow through an infinitely long pipe (see Larson et al. [6]). Some components of the numerical scheme we present here are based on the numerical scheme developed by the authors when studying the 2D flow past a cylinder in a channel [7]. Due to the wealth of studies available for this benchmark problem, the reader is referred to an early review of Tanner et al. [8] and a detailed literature survey in the monograph of Owens and Phillips [3] as well as a more recent overview in Faroughi et al. [9]. Historically, the problem has been incredibly difficult to solve computationally for two principal reasons. Firstly, the polynomial approximation functions associated with a particular numerical scheme are unable to capture the exponential profile of high Weissenberg number viscoelastic flow. This will cause the propagation of numerical errors in time. Secondly, normal stresses caused by elasticity on the surface of the sphere are propagated downstream and lead to viscoelastic instabilities. This results in a critical Weissenberg number, beyond which numerical solutions fail to converge. Dou and Phan-Thien [10] presented a theory explaining the viscoelastic instability by identifying an energy ratio I as a critical parameter for predicting the onset of this behaviour. The value of I is directly linked to the pressure gradient, which will cause the pressure within the shear layer on the cylinder to be much larger than the outside when a critical value of Wi is exceeded. A velocity inflection is then formed which results in the onset of instabilities in the numerical scheme.

Multi-phase axisymmetric viscoelastic flow is a broad and vibrant field of research. Recently, Turkoz et al. [11] and Zinelis et al. [12] simulated pressure induced viscoelastic jets, while Rubio et al. [13] investigated viscoelastic filament stretching and its possible application as an electrical conductor. The standard level set method was used in a finite element model to study viscoelastic two-fluid flow [14]. Additionally Amani et al. [15] used a conservative level set based finite volume framework to model viscoelastic droplet impact and flow through contractions / expansions using the log conformation formulation. The rise of an axisymmetric bubble in a viscoelastic fluid is one of the enduring multi-phase benchmark problems in computational rheology. Pioneering experimental and theoretical works by Astarita and Apuzzo [16] and Saffman et al. [17] were initiated back in the 1950s and 1960s, with the hypotheses that they posed still not satisfactorily resolved. The primary focus of this paper and most contemporary research in the field is to gain an understanding of the mechanism that causes the 'jump discontinuity' phenomenon. This occurs when the terminal rise velocity of a bubble experiences a discontinuity when plotted against bubble volume. The volume at which this discontinuity occurs is called the critical volume and varies depending on the type of viscoelastic fluid. The trailing cusp and negative wake are other characteristics of this problem that seem to contribute to the jump discontinuity since without them the phenomenon does not occur. The paper of Astarita and Apuzzo initially remarked that the trailing cusp shape was the primary factor behind the formation of the velocity jump, but this was later found not to be the case in the numerical study of Liu et al. [18] and the experimental work of Pilz and Brenn [19]. As the bubble rises, the velocity field in the wake is directed in the opposite direction to the rise, forming the negative wake structure. At one time this was thought to be the main cause of the jump but studies have shown the existence of one mechanism without the other [20]. Recently Bothe et al. [21] performed an investigation into the distribution of the circumferential

normal component of the polymeric stress tensor along the interface of the bubble and subsequently defined a unique mechanism to explain the velocity jump. This is explored in this paper using an axisymmetric formulation.

As previously mentioned, an axisymmetric geometric framework is used in this paper. This framework extends and builds on the computational model developed in a previous paper by the authors [7] for 2D planar flows. Making the assumption of axisymmetry harnesses the efficiency of planar simulations while retaining the ability to capture real world physical behaviour in three dimensions. The axisymmetric formulation of the governing equations for viscoelastic fluids is described by Kynch [22] while the implementation of the log-conformation formulation in this framework is novel. There is a wealth of research in viscoelastic flow that utilises an axisymmetric assumption for efficient computation. For example, Venkatesan et al. [23] presented an axisymmetric arbitrary Lagrangian-Eulerian (ALE) scheme for simulating viscoelastic rising bubbles and Rezaie et al. [24] investigated viscoelastic droplet impact onto thin films.

The novelty of this paper pertaining to single-phase flow is with respect to the further development of the understanding of the viscoelastic instability and its associated critical Weissenberg number for flow past a sphere. The inclusion of shear-thinning dynamics is investigated through use of the Giesekus model and compared with the Oldroyd B model. This work expands on the work of Claus et al. [25] who considered a planar formulation, and of Knechtges [26] who only considered Weissenberg number up to 15 for the Giesekus model. In this paper, numerical results are presented up to $\mathrm{Wi} = 100$. The dependence of the drag on the sphere on Wi and the Giesekus mobility factor is presented. Additionally, detailed contour plots are provided for the polymeric stress and the pressure fields to aid the discussion of the velocity inflection. The log-conformation formulation of Fattal and Kupferman [27] is utilised, enabling the HWNP to be circumvented. This solves the problem of the inability of polynomial basis functions to capture the exponential profile of polymeric stress and enables numerical results to be generated for Weissenberg numbers not currently available in the literature.

The novelty of the multi-phase framework used for simulating viscoelastic rising bubbles includes the conservative level-set method originally proposed by Olsson et al. [28]. This method itself is an extension of the original level-set method of Osher et al. [29]. The viscoelastic stresses that build up on the interface mean that mass conservation between the different phases of flow is crucially important. The use of non-conservative methods results in diffusion and eventual disappearance of one of the phases. The continuum surface force approach of Brackbill et al. [30] is used to model surface tension as a body force in the momentum equation and the diffused interface approach of Xie et al. [31] is used to calculate curvature while avoiding spurious velocities. This is the first time the diffused interface approach has been applied to the conservative level set method, being adapted from the VOF context in which it was implemented by Xie et al. [31]. The proposed multi-phase computational framework in this paper is benchmarked against the experimental results of Hnat and Buckmaster [32] to validate the numerical scheme. To the best of our knowledge, the conservative level-set method is combined with the log-conformation formulation of the constitutive equation within a finite element framework for the first time to create a stable and accurate state-of-the-art numerical scheme. This scheme is used to simulate bubbles rising in Newtonian and viscoelastic fluids for a wide range of initial bubble volumes to provide an interpretation on the unifying mechanism behind the velocity jump. To achieve this, 3D plots are presented for the bubble interface overlaid with axisymmetric slices of different fields. The velocity field is visualised between sub- and super-critical bubble volumes in order to identify the negative wake. Additionally, the normal components of the polymeric stress tensor are compared across different bubble volumes and instances of time.

The computational work is implemented in the FEniCS project [33], an open-source fully parallelised Python package which has been used to implement the specific formulations of all the equations presented in this paper. The back end of the FEniCS project framework is written entirely in C++, making simulations highly optimised. Additionally, a high performance computing cluster is used by the authors for all results given.

The remainder of the paper is structured as follows. Section 2 introduces the mathematical formulation of the governing equations and the equations that describe the conservative level-set method. Section 3 provides a description of the spatial and temporal discretisations of these equations. Section 4 is dedicated to single-phase flow and presents results for axisymmetric viscoelastic flow past a sphere in a pipe. Section 5 is concerned with multi-phase flow for a bubble rising in both Newtonian and viscoelastic fluids. Concluding remarks are made in Section 6.

2. Mathematical formulation

2.1. Governing equations

In this paper the governing equations for axisymmetric flow are formulated in a cylindrical polar co-ordinate frame (r, z, θ). The continuity and momentum equations are

$$\nabla \cdot \mathbf{u} = 0 \tag{1}$$

$$\rho\left(\frac{\partial \mathbf{u}}{\partial t} + (\mathbf{u}\cdot\nabla)\,\mathbf{u}\right) = \nabla\cdot\boldsymbol{\sigma} + \mathbf{F} \tag{2}$$

where $\mathbf{u} = (u_r, u_z, 0)^T$ is the velocity, ρ is the density and $\mathbf{F} = \mathbf{F}_g + \mathbf{F}_\sigma$ is the body force comprising the force due to gravity $\mathbf{F}_g = \rho\mathbf{g}$ and the force due to surface tension $\mathbf{F}_\sigma$ (see Section 2.3). In addition $\boldsymbol{\sigma}$ is the Cauchy stress tensor, given by

$$\boldsymbol{\sigma} = -p\mathbf{I} + 2\eta_s\mathbf{D}(\mathbf{u}) + \boldsymbol{\tau} \tag{3}$$

where p is the pressure, η_s is the solvent viscosity, $\mathbf{D}(\mathbf{u}) = \frac{1}{2}\left(\nabla\mathbf{u} + \nabla\mathbf{u}^T\right)$ is the rate-of-strain tensor and $\boldsymbol{\tau}$ is the polymeric stress tensor. This latter tensor can be expressed in terms of the conformation tensor $\mathbf{c}$ as follows

$$\boldsymbol{\tau} = \frac{\eta_p}{\lambda(1-\zeta)}(\mathbf{c} - \mathbf{I}) \tag{4}$$

where η_p is the polymeric viscosity, λ is the relaxation time and ζ is the slip parameter. The constitutive equation for $\mathbf{c}$ is

$$\frac{\partial \mathbf{c}}{\partial t} + \mathbf{u}\cdot\nabla\mathbf{c} - \mathbf{E}^T\cdot\mathbf{c} - \mathbf{c}\cdot\mathbf{E} = -\frac{(\mathbf{c}-\mathbf{I})}{\lambda} f(\mathbf{c}) \tag{5}$$

where $\mathbf{E} = \nabla\mathbf{u} - \zeta\mathbf{D}(\mathbf{u})$. The slip parameter is associated with the exponential Phan-Thien-Tanner (ePTT) model and characterises the degree to which the polymer chains within the fluid exhibit a non-affine response. When $\zeta = 0$, the response to deformation becomes affine and the left-hand-side of Eq. (5) simplifies to the upper convected derivative. This is the case for both the Oldroyd B and Giesekus models. The tensor function $f(\mathbf{c})$ is model dependent. In particular, we have

$$f(\mathbf{c}) = \begin{cases} \mathbf{I} & \text{Oldroyd B model} \\ \mathbf{I} + \alpha(\mathbf{c}-\mathbf{I}) & \text{Giesekus model} \\ \exp\left(\frac{\kappa_e}{1-\zeta}(\mathrm{tr}(\mathbf{c})-3)\right)\mathbf{I} & \text{ePTT model} \end{cases} \tag{6}$$

where α is the Giesekus mobility factor and κ_e is a model parameter. The conformation tensor $\boldsymbol{c}$ has the following representation:

$$\boldsymbol{c} = \begin{bmatrix} c_{rr} & c_{rz} & 0 \\ c_{rz} & c_{zz} & 0 \\ 0 & 0 & c_{\theta\theta} \end{bmatrix} \tag{7}$$

The governing equations written in component form can be found in Appendix A.

2.2. Log-conformation formulation

Since the conformation tensor $\mathbf{c}$ is symmetric positive definite we can determine its spectral decomposition. Let $\boldsymbol{\Lambda}$ be the diagonal matrix containing the eigenvalues λ_1, λ_2, λ_3, of $\mathbf{c}$. Let $\mathbf{R}$ be the matrix whose columns are the corresponding eigenvectors. The spectral decomposition is defined as

$$\mathbf{c} = \mathbf{R}\boldsymbol{\Lambda}\mathbf{R}^{\mathrm{T}} \tag{8}$$

We can then use a law of matrix logarithms to define the logarithm of the conformation tensor $\boldsymbol{\psi}$

$$\boldsymbol{\psi} = \ln\mathbf{c} = \mathbf{R}\ln(\boldsymbol{\Lambda})\mathbf{R}^{\mathrm{T}} \tag{9}$$

In order to derive an evolution equation for $\boldsymbol{\psi}$, we consider the following decomposition of the velocity gradient:

$$\nabla\mathbf{u} = \boldsymbol{\Omega} + \mathbf{B} + \mathbf{N}\mathbf{c}^{-1}, \tag{10}$$

where $\boldsymbol{\Omega}$ and $\mathbf{N}$ are anti-symmetric, and $\mathbf{B}$ is symmetric, traceless and commutes with $\mathbf{c}$, and where all tensors introduced in Eq. (10) depend on $\nabla\mathbf{u}$ and $\mathbf{c}$. Upon substitution of Eq. (10) into Eq. (5) we obtain

$$\frac{\partial \mathbf{c}}{\partial t} + \mathbf{u}\cdot\nabla\mathbf{c} - (\boldsymbol{\Omega}\cdot\mathbf{c} + \mathbf{c}\cdot\boldsymbol{\Omega}) - 2\mathbf{B}\cdot\mathbf{c} = -\frac{(\mathbf{c}-\mathbf{I})}{\lambda} f(\mathbf{c}) \tag{11}$$

We are now in a position to use Eq. (9) to rewrite Eq. (11) in terms of $\boldsymbol{\psi}$

$$\frac{\partial \boldsymbol{\psi}}{\partial t} + \mathbf{u}\cdot\nabla\boldsymbol{\psi} - (\boldsymbol{\Omega}\cdot\boldsymbol{\psi} - \boldsymbol{\psi}\cdot\boldsymbol{\Omega}) - 2\mathbf{B} = -\frac{(1-e^{-\psi})}{\lambda} f(e^{\psi}) \tag{12}$$

The details of this derivation can be found in Fattal and Kupferman [27]. It remains to show how the rotation and extension tensors $\boldsymbol{\Omega}$ and $\mathbf{B}$ are constructed. They are formed from the eigenvalues of the conformation tensor and the entries of the decomposition of the velocity gradient, and constructed in such a way that they satisfy the structures of the tensors in Eq. (10).

The eigenvalues of $\mathbf{c}$ are expressed in the form

$$\lambda_1, \lambda_2 = \frac{\mathrm{tr}(\mathbf{c}) \mp \sqrt{(c_{zz} - c_{rr})^2 + 4c_{rz}^2}}{2} \tag{13}$$

$$\lambda_3 = \mathrm{tr}(\mathbf{c}) - \lambda_1 - \lambda_2 \tag{14}$$

and the spectral decomposition of $\boldsymbol{\psi}$ is, by Eq. (9)

$$\boldsymbol{\psi} = \mathbf{R}\begin{bmatrix} \ln(\lambda_1) & 0 & 0 \\ 0 & \ln(\lambda_2) & 0 \\ 0 & 0 & \ln(\lambda_3) \end{bmatrix}\mathbf{R}^{\mathrm{T}} \tag{15}$$

The eigenvector associated with the eigenvalue λ_1 is given as follows:

$$\hat{\mathbf{v}}_1 = \begin{bmatrix} \lambda_1 - c_{zz} \\ c_{rz} \\ 0 \end{bmatrix} \tag{16}$$

and the corresponding normalised eigenvector is simply $\mathbf{v}_1 = \hat{\mathbf{v}}_1/|\hat{\mathbf{v}}_1|$. The matrix of eigenvectors $\mathbf{R}$ is then calculated as follows

$$\mathbf{R} = \begin{bmatrix} \mathbf{v}_{11} & -\mathbf{v}_{12} & 0 \\ \mathbf{v}_{12} & \mathbf{v}_{11} & 0 \\ 0 & 0 & 1 \end{bmatrix} \tag{17}$$

Define an intermediate tensor $\mathbf{M}$

$$\mathbf{M} = \begin{bmatrix} M_{rr} & M_{rz} & 0 \\ M_{zr} & M_{zz} & 0 \\ 0 & 0 & M_{\theta\theta} \end{bmatrix} = \mathbf{R}^{\mathrm{T}} \left(\nabla \mathbf{u} - \zeta \mathbf{D}(\mathbf{u})\right) \mathbf{R} \tag{18}$$

The extensional component $\mathbf{B}$ of Eq. (10) can now be defined as follows

$$\mathbf{B} = \mathbf{R} \begin{bmatrix} M_{rr} & 0 & 0 \\ 0 & M_{zz} & 0 \\ 0 & 0 & M_{\theta\theta} \end{bmatrix} \mathbf{R}^{\mathrm{T}} \tag{19}$$

We now introduce the scalar parameter ω:

$$\omega = \frac{\lambda_2 M_{rz} - \lambda_1 M_{zr}}{\lambda_2 - \lambda_1} \tag{20}$$

which is used in the construction of the rotational component $\boldsymbol{\Omega}$ of Eq. (10) as follows

$$\boldsymbol{\Omega} = \mathbf{R} \begin{bmatrix} 0 & \omega & 0 \\ -\omega & 0 & 0 \\ 0 & 0 & 0 \end{bmatrix} \mathbf{R}^{\mathrm{T}} \tag{21}$$

In Eq. (9), the rotation term on the left-hand-side is written in the form

$$\boldsymbol{\Omega} \cdot \boldsymbol{\psi} - \boldsymbol{\psi} \cdot \boldsymbol{\Omega} = \mathbf{R} \begin{bmatrix} 0 & \hat{\omega} & 0 \\ -\hat{\omega} & 0 & 0 \\ 0 & 0 & 0 \end{bmatrix} \mathbf{R}^{\mathrm{T}} \tag{22}$$

where scalar parameter $\hat{\omega} = \left(\ln(\lambda_2) - \ln(\lambda_1)\right) \omega$. In the limit where $\lambda_1 = \lambda_2$, we set

$$\hat{\omega} = \lim_{\lambda_1 \to \lambda_2} \left(\ln(\lambda_2) - \ln(\lambda_1)\right) \omega = M_{rz} - M_{zr} \tag{23}$$

Due to the inverse relationship between $\mathbf{c}$ and $\boldsymbol{\psi}$, the calculation of the source term is straightforward.

2.3. Conservative level-set method

The conservative level-set function ϕ is defined over the domain Ω as a continuous Heaviside function

$$\phi(\mathbf{x}) = \frac{1}{1 + e^{\hat{\phi}(\mathbf{x})/\epsilon}} \tag{24}$$

where $\hat{\phi}$ is a signed distance function and ϵ is a measure of interface thickness, chosen to depend on the spatial resolution of the computational mesh. The location of the interface Γ is given by the $\phi = 0.5$ contour. The 0 conservative level-set corresponds to phase 1 i.e. if $\phi = 0$ then $\mathbf{x} \in \Omega_1$, and the 1 conservative level-set corresponds to phase 2 i.e. if $\phi = 1$ then $\mathbf{x} \in \Omega_2$. Using this notation, we associate material parameters with individual phases of the flow

$$\rho(\phi) = \rho_2 \phi + \rho_1 (1 - \phi) \tag{25}$$

$$\eta_s(\phi) = \eta_{s,2} \phi + \eta_{s,1} (1 - \phi) \tag{26}$$

We then advect ϕ according to the velocity field $\mathbf{u}$

$$\frac{\partial \phi}{\partial t} + \mathbf{u} \cdot \nabla \phi = 0 \tag{27}$$

and reinitialise the profile of the conservative level-set function using

$$\frac{\partial \phi}{\partial \tau_1} + \nabla \cdot (\phi(1-\phi)\mathbf{n}) = \epsilon \nabla \cdot (\nabla \phi) \tag{28}$$

where $\mathbf{n} = \frac{\nabla \phi}{|\nabla \phi|}$ is the normal to the level-set function at the continuous level and τ_1 is an artificial time.

The force due to surface tension $\mathbf{F}_\sigma$ introduced in Section 2.1 is given as follows:

$$\mathbf{F}_\sigma = -\sigma \kappa \nabla \phi \tag{29}$$

where σ is the surface tension coefficient and $\kappa = \nabla \cdot \mathbf{n}$ is the curvature of the interface. We refer to Brackbill et al. [30] and Doherty et al. [7] for more details on the continuum surface force approach and its implementation. The calculation of the curvature often produces spurious oscillations which adversely affect the stability of the numerical scheme. In order to ensure a stable normal calculation, we follow the diffuse interface approach of Xie et al. [31] and solve the following diffusion equation

$$\frac{\partial \phi_D}{\partial \tau_2} = D \nabla^2 \phi_D, \tag{30}$$

where τ_2 is an artificial time and D is a mesh dependent diffusion coefficient. The initial condition for Eq. (30) is the solution of Eq. (27) i.e. $\phi_{D,0} = \phi$. The curvature described in the surface tension body forcing term (29) is now calculated using the diffused level set function from Eq. (30). This means the solution ϕ_D of Eq. (30) is used to calculate $\mathbf{n} = \frac{\nabla \phi_D}{|\nabla \phi_D|}$ which in turn is used to find a new curvature termed $\kappa_D = \nabla \cdot \mathbf{n}$. Due to the tendency of the level-set reinitialisation equation (28) to become unstable due to its non-linearity, it is advantageous to use this diffused level-set before performing the L^2 projection of the normal (see Section 3.1). The solution to the diffusion equation is used solely for calculating the unit normal vector $\mathbf{n} = \frac{\nabla \phi_D}{|\nabla \phi_D|}$ and is not used to modify the conservative level set function at any point in the simulation. This ensures that, the phase volume is conserved as before. Additionally, the diffusion coefficient D and time step $\Delta \tau_2$ are chosen to be of the order of the spatial resolution i.e. $O(h)$. This is because it is not possible to capture the complex hydrodynamic phenomena at the interface if the interface is too diffuse due to a highly inaccurate calculation of the normal.

2.4. Non-dimensional system

The governing equations can be summarised as follows

$$\begin{cases} \nabla \cdot \mathbf{u} = 0 \\ \rho \left(\dfrac{\partial \mathbf{u}}{\partial t} + (\mathbf{u} \cdot \nabla)\mathbf{u} \right) = \nabla \cdot \boldsymbol{\sigma} + \mathbf{F} \\ \boldsymbol{\sigma} = -p\mathbf{I} + 2\eta_s \mathbf{D}(\mathbf{u}) + \dfrac{\eta_p}{\lambda(1-\zeta)} \left(e^{\boldsymbol{\psi}} - \mathbf{I} \right) \\ \mathbf{F} = \rho \mathbf{g} + -\sigma \kappa_D \nabla \phi \\ \dfrac{\partial \boldsymbol{\psi}}{\partial t} + \mathbf{u} \cdot \nabla \boldsymbol{\psi} - (\boldsymbol{\Omega} \cdot \boldsymbol{\psi} - \boldsymbol{\psi} \cdot \boldsymbol{\Omega}) - 2\mathbf{B} = -\dfrac{(1 - e^{-\boldsymbol{\psi}})}{\lambda} f(e^{\boldsymbol{\psi}}) \end{cases} \tag{31}$$

The governing equations are written in non-dimensional form using the same scales used in Doherty et al. [7]. This yields the following system of equations

$$\begin{cases} \nabla \cdot \mathbf{u} = 0 \\ \rho \left(\dfrac{\partial \mathbf{u}}{\partial t} + (\mathbf{u} \cdot \nabla)\mathbf{u} \right) = \nabla \cdot \boldsymbol{\sigma} + \mathbf{F} \\ \boldsymbol{\sigma} = -p\mathbf{I} + \frac{2\beta}{\mathrm{Re}} \mathbf{D}(\mathbf{u}) + \dfrac{(1-\beta)}{\mathrm{ReWi}(1-\zeta)} \left(e^{\boldsymbol{\psi}} - \mathbf{I} \right) \\ \mathbf{F} = \frac{\rho \mathbf{g}}{\mathrm{Fr}^2} - \frac{1}{\mathrm{Eo}} \kappa_D \nabla \phi \\ \dfrac{\partial \boldsymbol{\psi}}{\partial t} + \mathbf{u} \cdot \nabla \boldsymbol{\psi} - (\boldsymbol{\Omega} \cdot \boldsymbol{\psi} - \boldsymbol{\psi} \cdot \boldsymbol{\Omega}) - 2\mathbf{B} = -\dfrac{(1 - e^{-\boldsymbol{\psi}})}{\mathrm{Wi}} f(e^{\boldsymbol{\psi}}) \end{cases} \tag{32}$$

where the Reynolds, Weissenberg, Froude and Eotvos numbers are defined as follows:

$$\mathrm{Re} = \frac{\rho_2 U L}{\eta_0}, \quad \mathrm{Wi} = \frac{\lambda U}{L}, \quad \mathrm{Fr} = \frac{U^2}{gL}, \quad \mathrm{Eo} = \frac{\rho_2 g L^2}{\sigma}. \tag{33}$$

Note that the non-dimensionalisation has been performed relative to the viscoelastic fluid. In addition to the governing equations in Eq. (32), we introduce a second system specifically for the conservative level-set equations

$$\begin{cases} \dfrac{\partial \phi}{\partial t} + \mathbf{u} \cdot \nabla \phi = 0 \\ \dfrac{\partial \phi}{\partial \tau_1} + \nabla \cdot (\phi(1-\phi)\mathbf{n}) = \epsilon \nabla \cdot (\nabla \phi) \\ \dfrac{\partial \phi_D}{\partial \tau_2} = D \nabla^2 \phi_D \end{cases} \tag{34}$$

where, it should be noted, there is no difference to the dimensional case.

3. Numerical discretisation

In this section the spatial and temporal discretisation of the systems of equations introduced in Section 2 are described. The finite element method is used to discretise in space with suitable choices of the relevant function spaces for the dependent variables. The coupling between the conservation of mass and momentum equations is crucial for the temporal discretisation and particular attention is given to this.

3.1. Spatial discretisation

When constructing the weak formulation of the problem, the trial and test function spaces must be chosen appropriately to ensure a well-posed problem. The computational domain is denoted by Ω and its boundary is Γ. The solution space for pressure is the function space $L^2_0(\Omega)$ defined by

$$L^2_0(\Omega) = \left\{ p \in L^2(\Omega) : \int_\Gamma p \, d\Omega = 0 \right\} \tag{35}$$

where the vanishing mean condition is necessary for the uniqueness of pressure. The solution space for velocity is $H^1_D(\Omega)$ where

$$H^1_D(\Omega) = \left\{ \mathbf{u} \in H^1(\Omega) : \mathbf{u}\big|_{\Gamma_D} = \mathbf{u}_D \right\} \tag{36}$$

where Γ_D is the portion of Γ on which Dirichlet boundary conditions are imposed. The final function space to define is $\left[L^2(\Omega)\right]^{3\times 3}_{\text{sym}}$, the space of symmetric 3×3 tensors with components in $L^2(\Omega)$.

3.1.1. Weak formulation of the governing equations

The Galerkin weak formulation of the system of PDEs defined in Eq. (32) is as follows. Find the triple $(p, \mathbf{u}, \boldsymbol{\psi}) \in L^2_0(\Omega) \times H^1_D(\Omega) \times \left[L^2(\Omega)\right]^{3\times 3}_{\text{sym}}$ such that

$$\begin{cases} \displaystyle\int_\Omega [\nabla \cdot \mathbf{u}] \cdot \xi_p \, d\Omega = 0 \\ \displaystyle\int_\Omega \left[\rho \left(\frac{\partial \mathbf{u}}{\partial t} + (\mathbf{u} \cdot \nabla)\mathbf{u} \right) \right] \cdot \xi_{\mathbf{u}} \, d\Omega = \int_\Omega [\nabla \cdot \boldsymbol{\sigma}] \cdot \xi_{\mathbf{u}} \, d\Omega + \int_\Omega \left[\frac{\rho \mathbf{g}}{\text{Fr}^2} + \mathbf{F}_\sigma \right] \cdot \xi_{\mathbf{u}} \, d\Omega \\ \boldsymbol{\sigma} = -p\mathbf{I} + \dfrac{2\beta}{\text{Re}} \mathbf{D}(\mathbf{u}) + \dfrac{(1-\beta)}{\text{ReWi}(1-\zeta)} \left(e^{\boldsymbol{\psi}} - \mathbf{I} \right) \\ \mathbf{F}_\sigma = -\dfrac{1}{\text{Eo}} \kappa_D \nabla \phi \\ \displaystyle\int_\Omega \left[\frac{\partial \boldsymbol{\psi}}{\partial t} + \mathbf{u} \cdot \nabla \boldsymbol{\psi} - (\boldsymbol{\Omega} \cdot \boldsymbol{\psi} - \boldsymbol{\psi} \cdot \boldsymbol{\Omega}) - 2\mathbf{B} \right] \cdot \xi_{\boldsymbol{\psi}} \, d\Omega + \\ \displaystyle\int_\Omega \frac{\gamma h}{|\mathbf{u}|^2} (\mathbf{u} \cdot \nabla \boldsymbol{\psi}) \cdot (\mathbf{u} \cdot \nabla \xi_{\boldsymbol{\psi}}) \, d\Omega = \int_\Omega \left[-\frac{(1-e^{-\psi})}{\text{Wi}} f(e^{\boldsymbol{\psi}}) \right] \cdot \xi_{\boldsymbol{\psi}} \, d\Omega \end{cases} \tag{37}$$

$\forall (\xi_p, \xi_{\mathbf{u}}, \xi_{\boldsymbol{\psi}}) \in L^2_0(\Omega) \times H^1_{D,0}(\Omega) \times \left[L^2(\Omega)\right]^{3\times 3}_{\text{sym}}$ where

$$H^1_{D,0}(\Omega) = \left\{ \mathbf{u} \in H^1(\Omega) : \mathbf{u}\big|_{\Gamma_D} = \mathbf{0} \right\} \tag{38}$$

The first term on the right-hand side of the second equation in (37) is evaluated non-trivially in the following way

$$\int_\Omega [\nabla \cdot \boldsymbol{\sigma}] \cdot \xi_{\mathbf{u}}\, d\Omega = \int_\Omega (\nabla \cdot \xi_{\mathbf{u}})\, p\, d\Omega - \int_\Omega \frac{2\beta}{\mathrm{Re}} \mathbf{D}(\mathbf{u}) : \mathbf{D}(\xi_{\mathbf{u}})\, d\Omega - \int_\Omega \frac{(1-\beta)}{\mathrm{ReWi}(1-\zeta)} \left(e^{\boldsymbol{\Psi}} - \mathbf{I}\right) : \mathbf{D}(\xi_{\mathbf{u}})\, d\Omega \tag{39}$$

The continuity and momentum equations are solved using a mixed finite element method with an appropriate choice of velocity and pressure basis functions to ensure stable approximations. In particular, the discrete velocity and pressure spaces must satisfy the Ladyzhenskaya–Babuška–Brezzi (LBB) condition. In this paper the $\mathbb{P}_2 - \mathbb{P}_1$ polynomial order pairing is used, which satisfies this condition. In addition to this mixed pairing we use $\mathbb{P}_2$ finite elements for the logarithm of the conformation tensor.

3.1.2. Weak formulation of the conservative level-set equations

The weak formulation of the conservative level-set equations (34) is: find $\phi \in L^2_0(\Omega)$ or $\phi_D \in L^2_0(\Omega)$ such that

$$\begin{cases} \displaystyle\int_\Omega \left[\frac{\partial \phi}{\partial t} + \mathbf{u} \cdot \nabla \phi\right] \cdot \xi_\phi\, d\Omega + \int_\Omega \frac{h}{|\mathbf{u}|^2} (\mathbf{u} \cdot \nabla \phi) \cdot (\mathbf{u} \cdot \nabla \xi_\phi)\, d\Omega = 0 \\ \displaystyle\int_\Omega \left[\frac{\partial \phi}{\partial \tau_1} + \nabla \cdot (\phi(1-\phi)\mathbf{n}) - \epsilon \nabla \cdot (\nabla \phi)\right] \cdot \xi_\phi\, d\Omega = 0 \\ \displaystyle\int_\Omega \left[\frac{\partial \phi_D}{\partial \tau_2} - D\nabla^2 \phi_D\right] \cdot \xi_\phi\, d\Omega = 0 \end{cases} \tag{40}$$

$\forall \xi_\phi \in L^2(\Omega)$. We also introduce the weak form of the L^2 projection of the normal to the interface: find $\mathbf{n} \in (L^2(\Omega))^2$ such that

$$\int_\Omega \left[\mathbf{n} - \frac{\nabla \phi_D}{|\nabla \phi_D|}\right] \cdot \xi_{\mathbf{n}}\, d\Omega = 0 \tag{41}$$

$\forall \xi_{\mathbf{n}} \in (L^2(\Omega))^2$ where it is important to note that the diffused level set calculated from the diffusion equation is used in the calculation of the normal. The numerical parameters are simulation dependent and will be given in Section 5. $\mathbb{P}_2$ finite elements are used for the discrete approximation to the level-set function and the normal to the interface.

3.1.3. SU/SUPG stabilisation method

Brooks and Hughes [34] noted that for convection dominated problems, the use of central difference schemes and Galerkin finite element methods produced spurious oscillations in the numerical solutions. The solution, found by Brooks and Hughes [34] and applied to viscoelastic flow problems by Marchal and Crochet [35] adds artificial diffusion into the problem by modifying the test function. The problem is no longer a Galerkin problem as the trial and test spaces no longer coincide. Given an arbitrary test function $\xi \in V$ where V is an arbitrary test space, we define the following modified test function:

$$\hat{\xi} = \xi + \frac{\gamma h}{|\mathbf{u}|^2} (\mathbf{u} \cdot \nabla \xi) \tag{42}$$

where γ is the upwinding parameter. There are two different stabilisation techniques that stem from this reformulation, the streamline-upwind (SU) and the streamline-upwind/Petrov-Galerkin (SUPG) methods. The former applies the test function given by Eq. (42) to only the convective term in the weak formulation of the constitutive equation. The latter applies the augmented test function to every term. In this paper we use the SU method for the viscoelastic constitutive equation (12) and the SUPG method for the conservative level-set advection equation (27).

3.2. Temporal discretisation

The Navier-Stokes equations require a discretisation which enables the continuity equation to be solved in conjunction with the momentum equation i.e. through a projection method. In the first step an intermediate velocity $\mathbf{u}_*$ is calculated using the following temporally discretised form of Eq. (2) and (3):

$$\frac{\rho(\mathbf{u}_* - \mathbf{u}_n)}{\Delta t} = -\rho(\mathbf{u}_n \cdot \nabla \mathbf{u}_*) + \nabla \cdot \boldsymbol{\sigma}_{*,n} + \mathbf{F}_n \tag{43}$$

$$\nabla \cdot \boldsymbol{\sigma}_{*,n} = -p_n \mathbf{I} + \frac{2\beta}{\mathrm{Re}} \mathbf{D}(\mathbf{u}_*) + \frac{(1-\beta)}{\mathrm{ReWi}(1-\zeta)} \left(e^{\boldsymbol{\Psi}_n} - \mathbf{I}\right) \tag{44}$$

The second step requires the solution of a Poisson equation for the pressure field at the next time-step p_{n+1}, ensuring continuity implicitly

$$\nabla^2 (p_{n+1} - p_n) = \frac{\rho}{\Delta t} \nabla \cdot \mathbf{u}_* \tag{45}$$

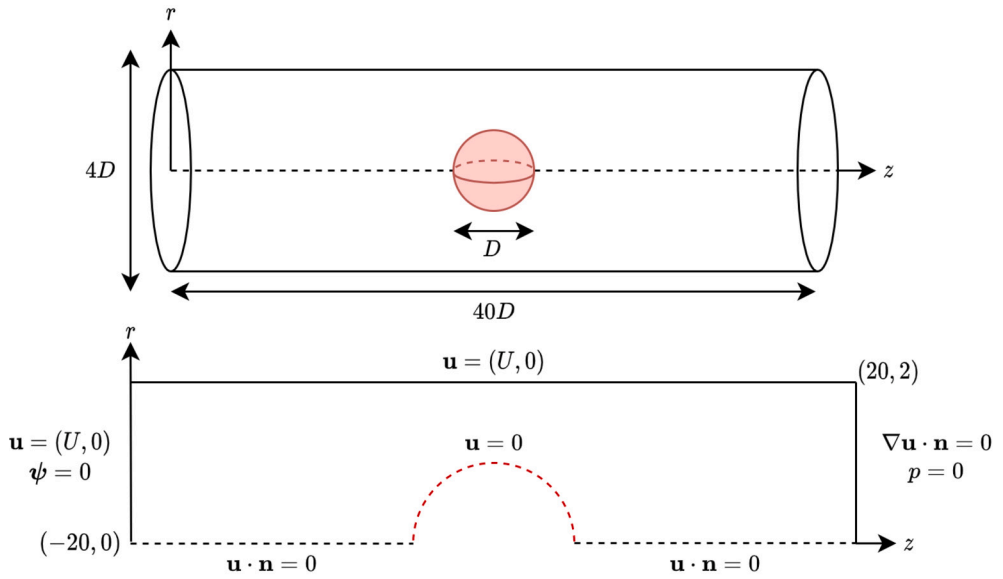

Fig. 1. Geometry and boundary conditions for the results in Section 4.

The final step is to calculate the correct velocity field $\mathbf{u}_{n+1}$ at the next time-step using the updated pressure field p_{n+1}:

$$\mathbf{u}_{n+1} - \mathbf{u}_* = \frac{\Delta t}{\rho} \nabla p_{n+1} \tag{46}$$

The time discretisation procedure for the constitutive equation is simply based on a 2nd-order accurate Crank-Nicolson implicit scheme:

$$\frac{\boldsymbol{\psi}_{n+1} - \boldsymbol{\psi}_n}{\Delta t} = \frac{1}{2} \left(\mathbf{C}(\boldsymbol{\psi}_{n+1}, \mathbf{u}_n) + \mathbf{C}(\boldsymbol{\psi}_n, \mathbf{u}_n) \right) \tag{47}$$

where

$$\mathbf{C}(\boldsymbol{\psi}, \mathbf{u}) = \mathbf{u} \cdot \nabla \boldsymbol{\psi} - (\boldsymbol{\Omega} \cdot \boldsymbol{\psi} - \boldsymbol{\psi} \cdot \boldsymbol{\Omega}) - 2\mathbf{B} + \frac{(1 - e^{-\Psi})}{\mathrm{Wi}} f(e^{\Psi}) \tag{48}$$

The level-set advection, reinitialisation and diffusion equations (27), (28), (30) are all solved using 1st-order implicit temporal schemes.

4. Single-phase flow

In this section we present results for creeping viscoelastic flow past a sphere. This is one of the most popular benchmark problems in computational rheology [36]. The quantities of interest are the drag on the sphere and the profiles of the polymeric stress on the axis of symmetry and the dependence of these on the Weissenberg number and mobility factor. We provide quantitative comparisons with the predictions of Knechtges [26] and Kynch and Phillips [22]. We assume there are no body forces so that $\mathbf{F} = 0$ and in the creeping flow regime $\mathrm{Re} = 0$.

The logarithm of the conformation tensor, $\boldsymbol{\psi}$, evolves according to the constitutive equation, with each iteration being used to create new pressure and velocity fields from the Stokes equations. The advantage of working in the Stokes regime is that solution of the mass and momentum equations is less computationally expensive.

The computational domain consists of a channel $\Omega = [-20, 20] \times [0, 2]$ obstructed by a sphere of radius $R = 1$ centred at the origin. A schematic of the computational domain can be viewed in Fig. 1. The boundary conditions for the problem are shown in Fig. 1 with the addition of a symmetry condition along the axis of symmetry. The domain is decomposed into a triangular mesh using the external mesh generation software Gmsh, where we make use of local mesh refinement techniques within the software to ensure a finer spatial discretisation near the surface of the sphere. This is visualised in Fig. 2.

4.1. Drag coefficient

The quantity of interest is the drag correction factor K

$$K = \frac{1}{6\pi\eta_0 RU} \int_{\Gamma_S} \mathbf{e}_z^T \cdot [-p\mathbf{I} + 2\beta\mathbf{D} + \boldsymbol{\tau}] \cdot \boldsymbol{n} \, dS \tag{49}$$

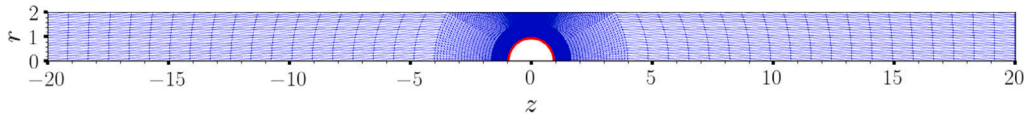

(a) Full mesh

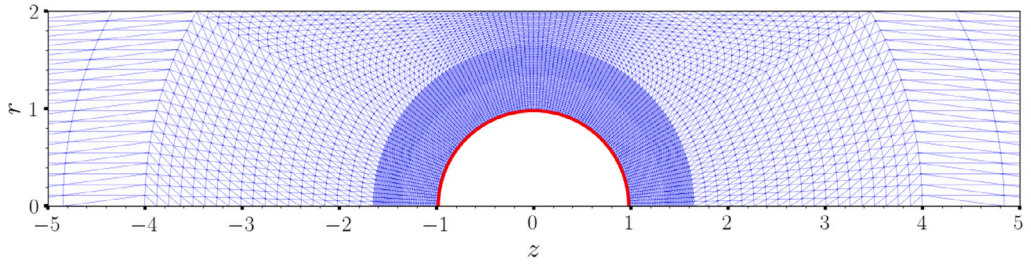

(b) Zoom around the sphere

Fig. 2. Mesh schematic for the results in Section 4.

Table 1
Dependence of the drag correction factor K on the Weissenberg number Wi and mobility factor α.

Wi	K							
	$\alpha = 0$		$\alpha = 0.001$		$\alpha = 0.01$		$\alpha = 0.1$	
	M	[22]	**M**	[26]	**M**	[26]	**M**	[26]
0.1	5.9046	5.9060	5.90354	5.90473	5.89453	5.89573	5.82046	5.82166
0.2	5.8067	5.8082	5.80301	5.80393	5.77184	5.77275	5.57068	5.57160
0.3	5.6928	5.6943	5.68530	5.68610	5.62606	5.62694	5.32273	5.32349
0.4	5.5845	5.5861	5.57253	5.57324	5.48393	5.48451	5.10722	5.10785
0.5	5.4902	5.4918	5.47303	5.47366	5.35488	5.35531	4.92437	4.92489
0.6	5.4116	5.4131	5.38855	5.38910	5.24100	5.24127	4.76896	4.76938
0.7	5.3475	5.3492	5.31813	5.31861	5.14106	5.14118	4.63584	4.63616
0.8	5.2966	5.2983	5.25991	5.26037	5.05281	5.05280	4.52084	4.52109
0.9	5.2563	5.2583	5.21178	5.21235	4.97399	4.97387	4.42072	4.42090
1	5.2243	5.2276	5.17174	5.17264	4.90268	4.90248	4.33290	4.33303
2	-	-	4.97518	-	4.41464	4.41375	3.82920	3.82914
5	-	-	-	-	3.84116	3.84040	3.40861	3.40864
15	-	-	-	-	3.42175	3.42218	3.16935	3.16952
35	-	-	-	-	3.24705	-	3.08415	-
100	-	-	-	-	3.12756	-	3.03136	-

where $\mathbf{e}_z$ is the unit vector in the z direction. We calculate K for a range of Weissenberg numbers and mobility factors and compare our predictions with the literature. We consider three different mobility factors, $\alpha = 0.001, 0.01, 0.1$, and for each we investigate flow dynamics for Weissenberg numbers in the small and large limits. We also consider the case when $\alpha = 0$ which corresponds to the Oldroyd B model. The viscosity ratio is $\beta = 0.5$ and the upwinding parameter is $\gamma = 0.05$ with simulations being run until the drag correction factor K reaches a steady state. We use a constant time step $\Delta t = 0.001$ and minimum mesh resolution of $h = 0.00396$ which we found was sufficient to achieve numerical convergence. This mesh will be referred to as **M**. As can be observed in Table 1 excellent agreement is observed with values from the literature (Kynch and Phillips [22] and Knechtges [26]). We have agreement of up to three decimal places for all values of K compared with the results for the Giesekus model in Knechtges [26], illustrating the power of the log-conformation formulation in simulating high Weissenberg number flows. The shear-thinning characteristics of the fluid increase with α. This explains the reduction in drag for large values of α as a reduction in viscosity in regions of high fluid velocity will reduce the stress on the sphere. As the mobility factor decreases and converges to the Oldroyd B model, simulations break down at much lower Weissenberg numbers. The scheme is stable up until Wi $= 2$ for $\alpha = 0.001$, improving on the range of values reported in Knechtges [26] who presented results up to Wi $= 1.6$. One reason for numerical breakdown is the very large viscoelastic stresses that are generated and these become increasingly difficult to resolve numerically. Another possibility for breakdown could be the unsuitability of the Oldroyd B model for flows that have a significant extensional component since there is a singularity in the extensional viscosity for this model. For the sake of completeness, we include in the far left column in Table 1 drag values for $\alpha = 0$ i.e. the Oldroyd B model. We compare with the results of Kynch and Phillips [22] who performed a parametric study investigating how the drag varied with respect to the viscosity ratio and Reynolds number, among other values. We observe excellent agreement with the literature and successfully validate our framework for the Oldroyd B model. For mobility factors $\alpha = 0.01$ and $\alpha = 0.1$ we have unconditional stability with respect to Wi.

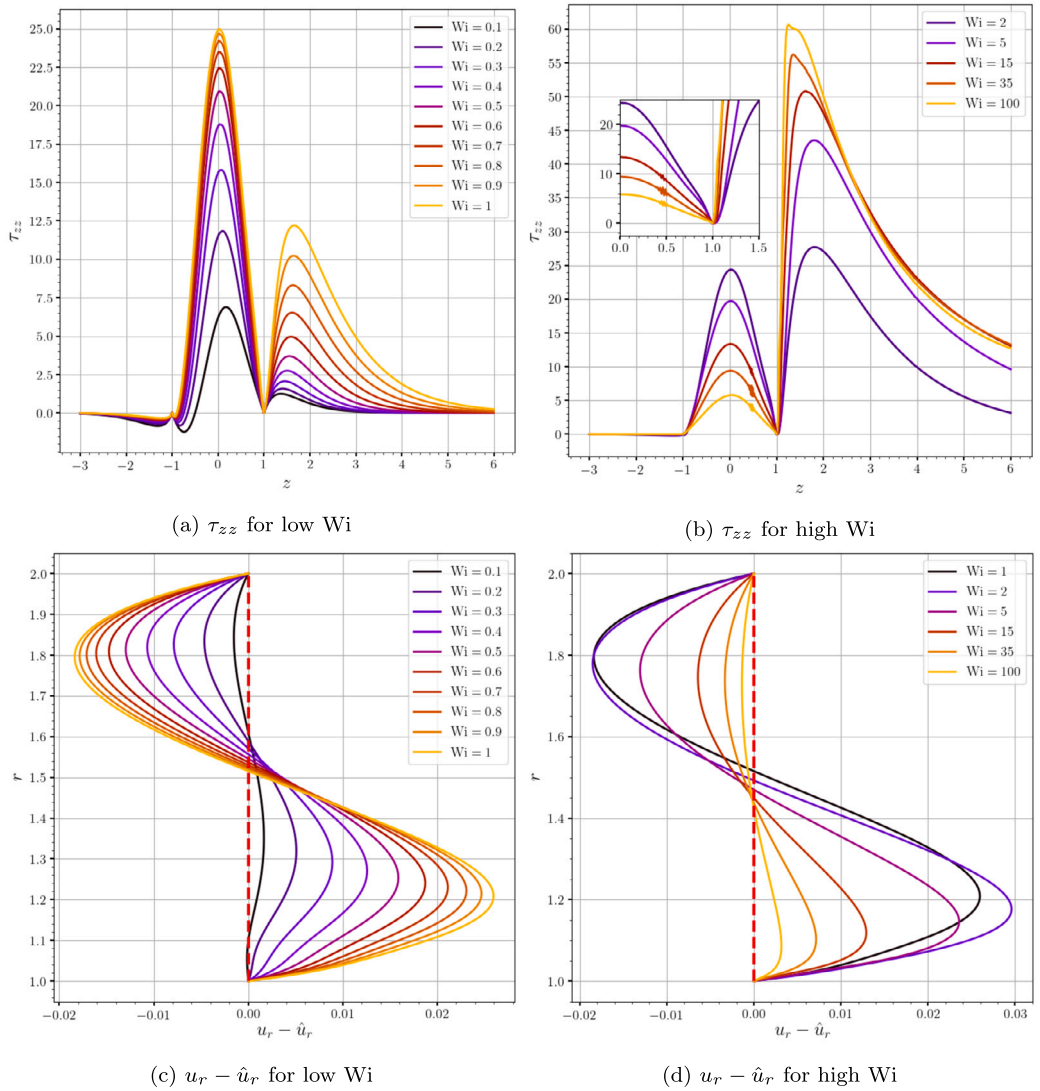

(a) τ_{zz} for low Wi

(b) τ_{zz} for high Wi

(c) $u_r - \hat{u}_r$ for low Wi

(d) $u_r - \hat{u}_r$ for high Wi

Fig. 3. Plots of τ_{zz} along $r = 0$ for $z \in [-3, 6]$ (Figs. 3a and 3b) and $u_r - \hat{u_r}$ along $z = 0$ for $r \in [1, 2]$ (Figs. 3c and 3d) for $\alpha = 0.01$. (For interpretation of the colours in the figure(s), the reader is referred to the web version of this article.)

4.2. Plots along paths

In Fig. 3 the axial normal polymeric stress component τ_{zz} and the difference between the viscoelastic radial velocity u_r and the Newtonian radial velocity $\hat{u_r}$ are analysed. In Figs. 3a and 3b τ_{zz} is plotted along $r = 0$ from $z = -3$ to $z = 6$, including the circumference of the sphere, for low and high values of Wi, respectively. The low interval runs from Wi $= 0.1$ to Wi $= 1$ with increments of 0.1 while the large range includes Wi $= 2$, 5, 15, 35 and 100. For both low and high Wi, the behaviour of τ_{zz} upstream of the sphere is very similar as the fluid has not undergone deformation. Along the circumference of the sphere, the polymeric stress increases with increasing Wi in the low limit but has the inverse relationship for the large limit, with τ_{zz} decreasing for increasing Wi. Moving downstream of the sphere, we observe similar behaviour in τ_{zz} in the low limit, with the polymeric stress gradually increasing with increasing Wi. The same behaviour is observed in the large limit, but now the polymeric stress reaches its maximum value downstream of the sphere rather than on the circumference of the sphere as it did in the low limit. This behaviour is observed for $2 \leq$ Wi ≤ 100. It would appear that the explanation for this behaviour is the increase in Weissenberg number correlates with an increase in elastic forces within the fluid which cause the polymer molecules to stay extended for longer. As viscoelastic stresses take time to build up fully, the peak value attained by τ_{zz} is transferred from the sphere surface to downstream in the wake with rising Wi. In addition to this finding, we observe that τ_{zz} converges to a maximum value of $\tau_{zz} \approx 25$ in the low limit. For Wi $= 2$ this value is maintained and then abruptly starts decreasing with rising Wi in the large limit. This suggests the existence of a turning point between Wi $= 2$ and Wi $= 5$ at which the overall value of τ_{zz} on the sphere surface decreases rather than increases with rising Wi.

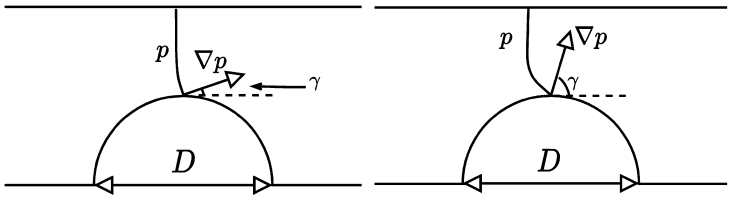

(a) Low Wi (b) High Wi

Fig. 4. Schematic picture illustrating how an increase in Wi can cause a change in the angle at which the pressure gradient meets the sphere surface, leading to a velocity inflection.

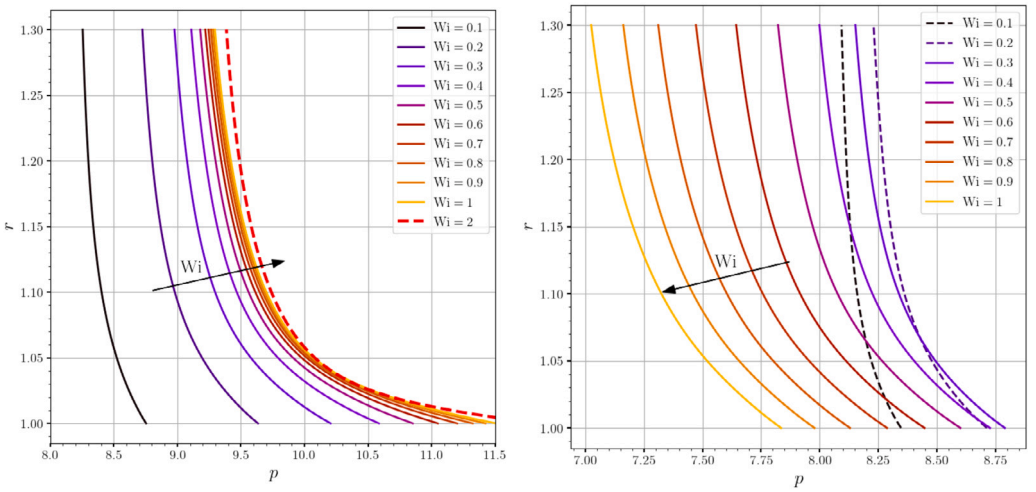

(a) Pressure p for $\alpha = 0.001$ (b) Pressure p for $\alpha = 0.1$

Fig. 5. Profiles of $p(r, 0)$, $1 \leq r \leq 1.3$, for (a) $\alpha = 0.001$ and (b) $\alpha = 0.1$, and $0.1 \leq \mathrm{Wi} \leq 1$.

Upon increasing the Weissenberg number, the polymeric stress gradients become increasingly small the closer we get to the surface of the sphere. As can be seen in Fig. 3b, there are small oscillations in the profile of τ_{zz} at $z = 0$ which are particularly noticeable for Wi = 35 and Wi = 100. Similar distortions in the stress profile for large Weissenberg numbers are visible downstream of the sphere. This is due to the increasingly large stresses generated along the axis of symmetry due to the large extensional rates and suggests finer mesh resolution is required in this region to resolve fully. Claus et al. [25] reported results with a similar overall physical interpretation as our own. Namely, Figure 5.8 in their simulations for the Oldroyd B viscoelastic model showed a constant increase in τ_{xx} for rising Wi in the low limit. These qualitative comparisons imply that similar interpretations can be made about the polymeric stress between 2D Cartesian and 3D axisymmetric simulations. In Figs. 3c and 3d we illustrate how the radial velocity profile fluctuates from its Newtonian counterpart on the $z = 0$ axis between $r = 1$ and $r = 2$ for Wi in the small and large limit. Fig. 3c indicates a larger departure from the Newtonian regime with increasing Wi, as expected. In both figures the viscoelastic profile is larger closer to the sphere surface and smaller closer to the upper channel wall. What can be discerned clearly is the difference $u_r - \hat{u}_r$ in Fig. 3c increases with increasing Wi. Furthermore, in Fig. 3d we reach a turning point between Wi = 2 and Wi = 5 where any further increase in Wi leads to a decrease in the difference. As a result, for Weissenberg numbers in the very large limit the radial profile appears to become more and more Newtonian. We attribute this to the decrease in polymeric stress seen in Fig. 3b which we can primarily attribute to shear-thinning behaviour of the Giesekus model.

Finally, we describe how the pressure p varies over the axis $z = 0$ between $r = 1$ and $r = 1.3$ and how this contributes to the onset of viscoelastic instability. Following from the work of Dou and Phan-Thien [10] and Claus et al. [25], the ratio of the energy gradient normal to the streamlines $\frac{\partial E}{\partial \mathbf{n}}$ and the energy dissipation gradient in the streamwise direction $\frac{\partial H}{\partial \mathbf{s}}$ is identified as a stability criterion for the flow. It is described as follows:

$$I = \frac{\partial E/\partial \mathbf{n}}{\partial H/\partial \mathbf{s}} = \frac{\frac{\partial p}{\partial r}}{\frac{1}{\hat{r}}\frac{\partial p}{\partial \hat{\theta}}} \tag{50}$$

where we recast our axisymmetric cylindrical co-ordinate system $(r, z, 0)$ into a two-dimensional polar co-ordinate frame $(\hat{r}, \hat{\theta})$. By exploiting basic trigonometry we note that I can be calculated by considering the vector given by the pressure gradient and taking the arctangent of the angle γ given by the components of ∇p (see Fig. 4). Fig. 5a displays how the pressure varies along $z = 0$ between $1 \leq r \leq 1.3$ with respect to $\alpha = 0.001$ and Weissenberg numbers in the low limit (0.1 - 1) and Wi = 2. As we can see the increase

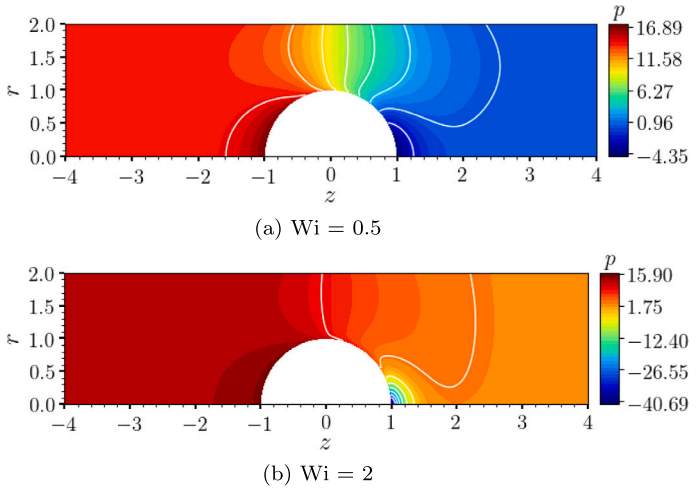

Fig. 6. Pressure contour plots for $\alpha = 0.001$: (a) Wi = 0.5, (b) Wi = 2.

in Wi corresponds to the angle γ increasing, which in turn increases the magnitude of I. This deformation of the pressure contour continues until Wi = 2 when our numerical scheme diverges. The convergence of the pressure contours for larger Weissenberg numbers in Fig. 5a indicates a limiting value of I exists for this problem, beyond which numerical schemes will diverge. The physical interpretation of the instability is that the extreme pressure variation leads to a velocity inflection on the top of the cylinder which is indicative of the conversion to a transient flow regime. Fig. 6 presents the pressure contour plots for $\alpha = 0.001$. We see in Fig. 6a for Wi = 0.5 that the pressure contours about the $z = 0$ axis are only slightly distorted. In comparison to Fig. 6a, the situation in Fig. 6b is quite different. The contour about $z = 0$ is very distorted, corresponding to a large value of γ and indicating the onset of viscoelastic instability. In fact, we believe the instability has already begun as the pressure is approaching a singularity on the downstream surface of the sphere. We concur with the findings of the literature and observe the same behaviour as being present in the axisymmetric problem for low mobility factors. As α increases we move further away from the instabilities associated with the Oldroyd B model and into the more stable Giesekus regime. As a result Fig. 5b displays the same Weissenberg numbers but now for $\alpha = 0.1$. Increasing Wi here corresponds to γ becoming smaller which indicates the flow is less likely to become unstable. This is supported by the data in Table 1 indicating stable solutions for this mobility factor up to Weissenberg number 100. To conclude, we observe that the main stabilising factor for viscoelastic flow past a sphere is the introduction of shear-thinning dynamics in the flow that act to suppress viscoelastic instabilities.

4.3. Contour plots

In Figs. 7 and 8 the contours of the axial normal polymeric stress τ_{zz} are presented. In the first of these, Fig. 7, we show how τ_{zz} varies for Wi = 0.1, 0.5 and 1 and $\alpha = 0.01$. As we established in Section 4.2, τ_{zz} reaches its maximum on the sphere surface in the low Wi limit. The value of this maximum also increases with increasing Wi and this behaviour can be clearly seen as well in Fig. 7. As the fluid deforms as it passes over the sphere, there is an increase of elastic stress. This elastic stress increases in magnitude as Wi increases since the fluid takes longer to return to its equilibrium state. Moreover, we can clearly see the formation of a stress boundary layer on the top of the sphere and also the formation of a smaller boundary layer on the upper channel wall. This is formed by fluid displaced by the sphere being impacted against the channel wall, increasing the polymeric stress in this region.

In Fig. 8, the value of Wi is fixed at Wi = 0.7 and the Giesekus mobility factor α is varied. Fig. 8b is the most similar to the results shown in Fig. 7, where the axial polymeric stress τ_{zz} is large and the subsequent stress contour extends far down into the wake. When α is increased from $\alpha = 0.01$ to $\alpha = 0.1$ the polymeric stress decreases everywhere as the fluid begins to relax. This is because the fluid becomes more inertia dominated and thins more rapidly due to shear. As expected, the reverse is true for when we decrease the mobility factor to $\alpha = 0.001$. In this case we approach the Oldroyd B model and the fluid becomes much less reactive to deformation dependent changes in viscosity. This means we have a more viscous fluid around the sphere which leads to an increase in the axial polymeric stress. This is especially noticeable on the surface of the sphere and the wall of the channel where stress boundary layers are formed.

5. Multi-phase flow

In this section, the multi-phase capability of our scheme is demonstrated, beginning with the 3D rising bubble benchmark problem of Hnat and Buckmaster [32]. Here we calculate rise velocities and inspect the interface of the bubble for both qualitative and quantitative confirmation. Next, we investigate the more complex case of axisymmetric viscoelastic rising bubble. Here we perform an analysis of the behaviour of these bubbles about critical volumes where a velocity jump discontinuity occurs. We validate our results by comparing the predicted rise velocities to those reported in the literature, namely the experimental work of Pilz et al.

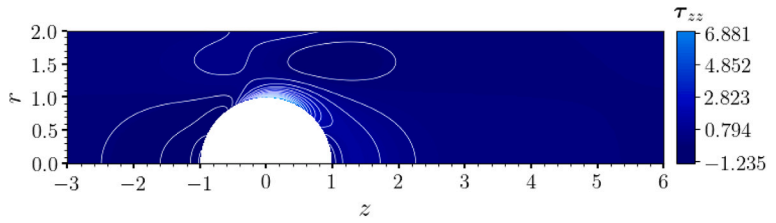

(a) $\alpha = 0.01$, Wi $= 0.1$

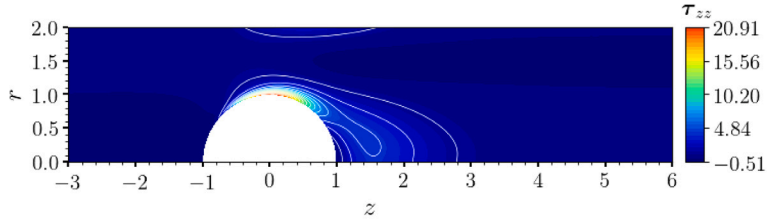

(b) $\alpha = 0.01$, Wi $= 0.5$

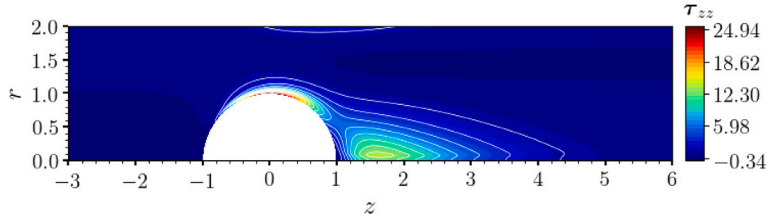

(c) $\alpha = 0.01$, Wi $= 1$

Fig. 7. Contour plots of the τ_{zz} component of the polymeric stress tensor for $\alpha = 0.01$ and different Weissenberg numbers.

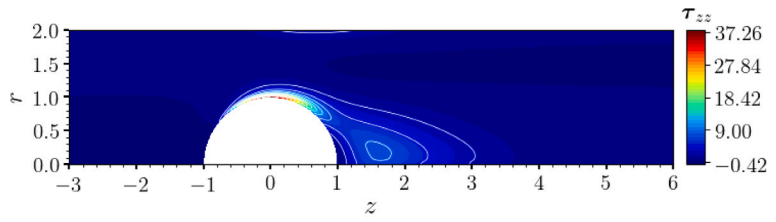

(a) $\alpha = 0.001$, Wi $= 0.7$

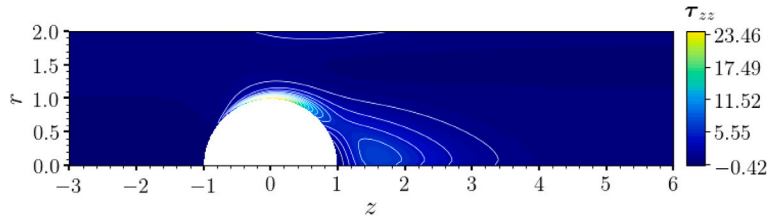

(b) $\alpha = 0.01$, Wi $= 0.7$

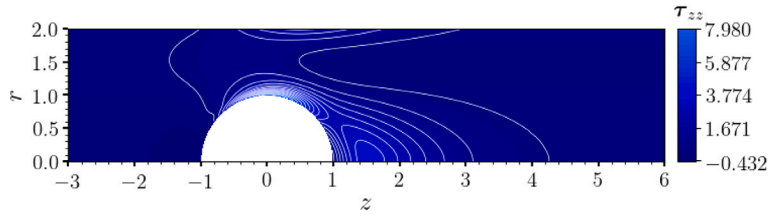

(c) $\alpha = 0.1$, Wi $= 0.7$

Fig. 8. Contour plots of the τ_{zz} component of the conformation tensor for Wi $= 0.7$ and different mobility factors.

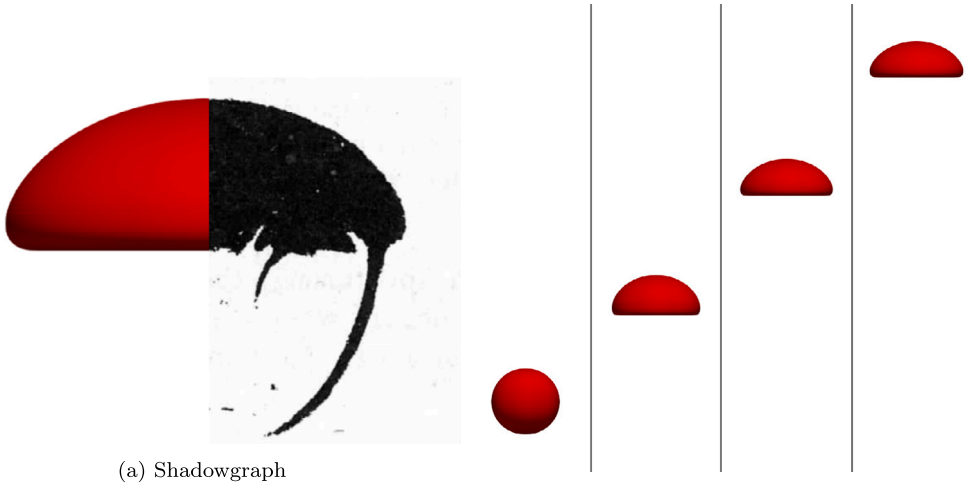

(a) Shadowgraph (b) Bubble during rise

Fig. 9. Comparison between experimental and numerical predictions for the 3D bubble shape described in Section 5.1. a): Shadowgraph image of the experimental results from Hnat and Buckmaster [32]. b): Snapshots of an axisymmetric Newtonian rising bubble.

[19] and the numerical work of Bothe et al. [21]. We also analyse other bubble metrics such as sphericity, the centroid and the bubble interface. Qualitative agreement is also observed by modelling the negative wake velocity field and comparing normal stress contours between sub- and super-critical bubble volumes.

5.1. Newtonian rising bubble

The conservative level-set method is validated by considering the benchmark problem of a 3D rising bubble in a column of Newtonian fluid. We use as a benchmark the experimental work conducted by Hnat and Buckmaster [32] who investigated bubbles rising in the spherical cap regime. The authors provided snapshots of bubble shapes and terminal rise velocities for a range of parameter sets. In particular, comparisons are made with case A in Table 1, a shadowgraph image shown in Fig. 9a. This experimental work has been used to validate a large number of other multi-phase flow codes including those of Gueyffier et al. [37], Yokoi [38], and Xie et al. [31].

The computational set-up is as follows: a bubble of radius R rises along the centre of a cylindrical pipe of radius $12R$ and height $18R$. A locally refined mesh is used for $x \leq 4R$ in order to guarantee a high degree of accuracy at low computational cost. In Fig. 9b we display snapshots of the bubble's rise from rest at $t = 0$ s until the end of the simulation time at $t = 0.3$ s. The bubble rises under the action of buoyancy and the interface deforms into a cap shape due to the balance between pressure, viscous stress and interfacial tension forces on the interface. The mesh convergence study has been carried out for four different mesh resolutions. In Fig. 10c the experimentally observed terminal rise velocity is depicted and good agreement is found with our simulations. The coarsest mesh has resolution $h = 0.1R$ and the finest mesh has $h = 0.00125R$ with mesh convergence to a terminal rise velocity of 21.5 cm/s. Fig. 10a shows that there is little variation in the evolution of the centre of mass with respect to mesh size which is to be expected due to the very small change in terminal rise velocity observed in Fig. 10c. Finally, the sphericity factor given by the following expression:

$$S = \frac{\text{surface area of volume equivalent sphere}}{\text{surface area of bubble}} = \frac{\left[(6V)^2\pi\right]^{\frac{1}{3}}}{A} \tag{51}$$

is a measure of how the bubble surface area differs from that of a perfect sphere, with $S = 1$ indicating no difference. This is explored for different spatial resolutions in Fig. 10b, where a decrease in h leads to a decrease in sphericity. This is due to an increase in refinement allowing bubble deformation to be captured more accurately.

5.2. Viscoelastic rising bubble

The viscoelastic fluid 0.8 wt.% Praestol 2500 is considered in this paper since it is the fluid that was used in the experimental work of Pilz et al. [19] to study bubble dynamics. The relevant material parameters for this fluid can be found in Table 1 of the aforementioned paper. In their experiments, a schematic of which can be viewed in Fig. 11b, a plexi-glass bubble generating chamber is attached below a larger test column in which the bubble rises. The ball valve is closed and liquid is removed from the chamber through a syringe and air rushes in through the capillary due to a pressure differential. The ball valve is then opened and the bubble is allowed to rise. The test column in which the viscoelastic fluid is contained measures 120 mm × 450 mm while the computational domain used in our work which is shown in Fig. 11a is a pipe of radius 30 mm and height 60 mm. The justification for the difference in scale is that extending the wall any further than 30 mm has negligible effects on bubble dynamics and 60 mm is high enough for

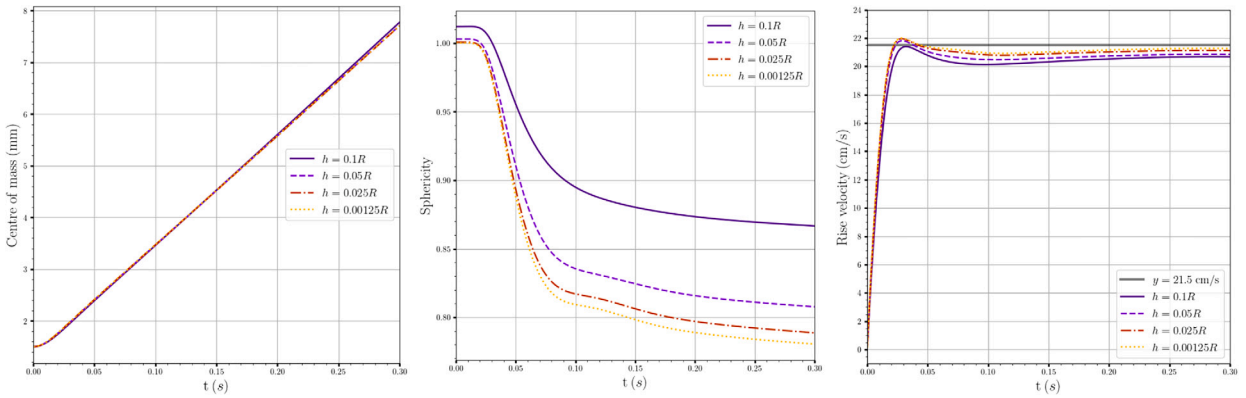

(a) Centre of mass (b) Sphericity (c) Rise velocity

Fig. 10. Bubble metrics for the axisymmetric Newtonian rising bubble benchmark in Section 5.1.

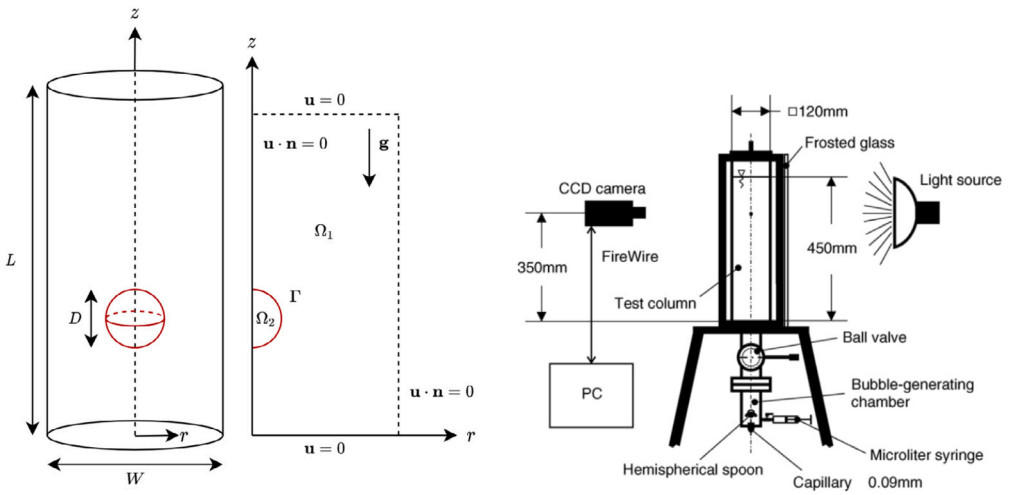

(a) Our numerical schematic (b) Experimental setup of Pilz et al. [19]

Fig. 11. Schematics of the computational and experimental setup.

all the bubbles in our test range to reach their terminal velocity. This experimental set up has been used in the fully 3D numerical simulations of Yuan et al. [39] and Bothe et al. [21]. While exact comparisons cannot be drawn between our axisymmetric work and these examples from the literature, it will be shown that much of the same hydrodynamic phenomena is still present.

The simulations begin with a spherical bubble initiated at $z = 10$ mm and terminate at a final time of $t = 0.4$ s. A time-step of $\Delta t = 0.208 \times 10^{-4}$ s is used. The exponential PTT constitutive model is used with parameter values $\zeta = 0.12$ and $\epsilon = 0.05$, chosen in line with those used in Niethammer et al. [40]. The viscoelastic fluid modelled is Praestol 2500 (PAM) 0.8 wt.%. Rheological experiments and viscometric analysis were performed by Pilz and Brenn [19] and Niethammer et al. [40] respectively. As such, the solvent and polymeric viscosities considered for the model are $\eta_s = 0.03$ Ns/m^2 and $\eta_p = 1.483$ Ns/m^2 which are the same as those used by Niethammer et al. [40]. The total viscosity of the fluid is then $\eta_0 = 1.513$ Ns/m^2 which is approximately the same as the experimentally measured value from Pilz and Brenn [19]. The solvent viscosity is chosen to be larger than the real solvent viscosity which is reported to be $\eta_s = 0.001$ Ns/m^2. The reason the solvent viscosity is increased to the value used here and also in Niethammer et al. [40] is to maintain stability in the momentum equation by not allowing the hyperbolic polymeric stress term to dominate. The constitutive and level-set advection equations are stabilised by the SU and SUPG methods, respectively, with an upwinding parameter of $\gamma = 0.1$. This value is chosen to be larger than the one used in the single phase results in Section 4 for stability. We impose the condition that for each bubble volume considered, its diameter satisfies $d = 120h$. For the interface, we use a thickness of $\varepsilon = \frac{5}{12}h$ and perform three reinitialisation iterations with timestep $\Delta\tau_1 = 0.1h$. To mitigate numerical errors when calculating the normal to the interface, we perform three diffusion iterations with time step $\Delta\tau_2 = 0.1h$ and use a diffusion coefficient of $D = 0.1h$. The effect of the choice of diffusion coefficient on the rise velocity and variation of bubble volume are shown in Fig. 12. As can be seen in Fig. 12 there is little variation in either the rise velocity or the volume of the bubble as a result of implementing the diffusion step. Furthermore, there is a minimal change as D is increased to $D = 0.2h$.

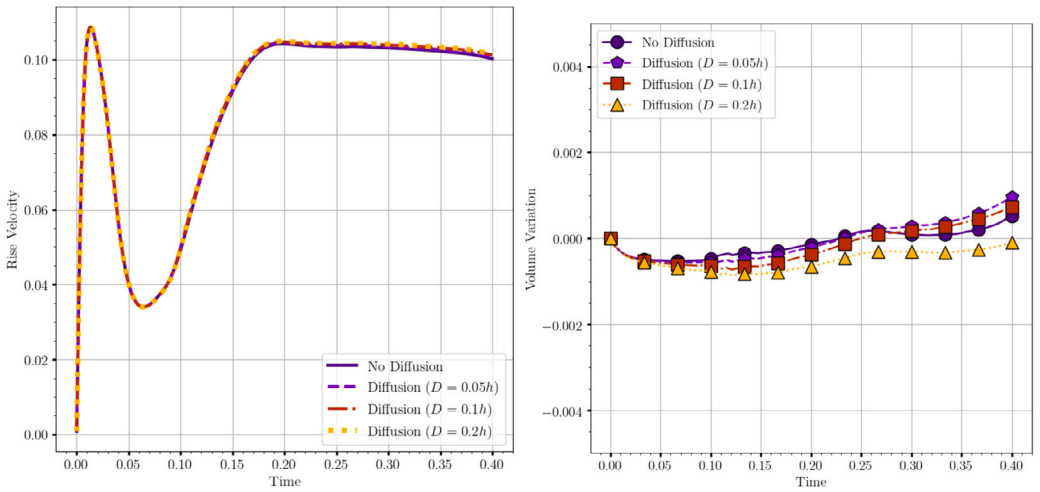

(a) Rise velocities (b) Volume variation

Fig. 12. Effect of the diffused interface approach for varying diffusion coefficients D on a viscoelastic rising bubble of volume $V = 70$ mm^3.

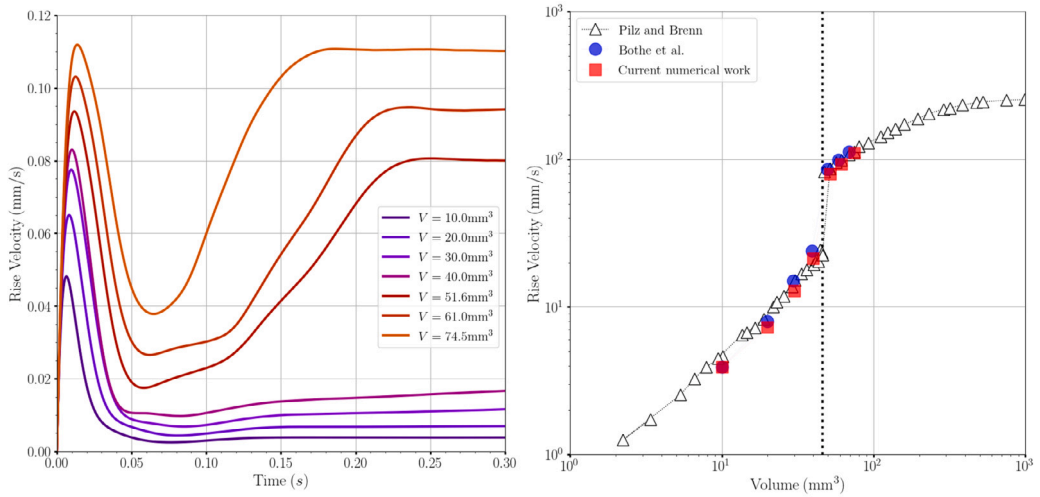

(a) Rise velocities (b) Terminal rise velocities

Fig. 13. (a) Influence of evolution of rise velocity on initial bubble volume, (b) comparison of dependence of steady state rise velocity on volume V with the experimental work of Pilz et al. [19] and the numerical simulations of Niethammer et al. [40] (reproduced by Bothe et al. [21]).

5.2.1. Bubble metrics

The most effective way of validating the accuracy of a numerical scheme when simulating viscoelastic rising bubbles is to take the volume averaged rise velocity and compare the terminal values to those gathered experimentally. These values can then be expressed on a log-log plot with volume on the x-axis and velocity on the y-axis, so that the jump discontinuity can be identified at the critical volume. Fig. 13a displays the rise velocities of all the bubbles in the range. For all bubbles the large increase in velocity at around $t = 0.01$ s is attributed to the dominant buoyancy forces. Exactly the same behaviour is exhibited in Newtonian fluids. Next, due to the increase in velocity and the fact that viscoelastic stresses have had enough time to build up, a rebound is exhibited where the rise velocity decreases to a local minimum dependent on bubble volume. This is observed to be around $t = 0.06$ s but varies slightly with bubble volume. Once the viscoelastic stresses relax and begin to accumulate along the interface, namely the cusp at the rear of the bubble, the subsequent rise is dependent on whether the volume is sub-critical or super-critical. For 0.8 wt.% Praestol 2500 the experimentally observed critical volume is found to be $V_c = 45.97957$ mm^3, represented by the black line in Fig. 13b. For bubbles with $V < V_c$ the bubble stays within a small region of this local minimum for the rest of its rise. On the other hand, for bubbles $V > V_c$ another elastic rebound takes place as the viscoelastic stresses accumulate and phenomenological activity within the viscoelastic fluid thrusts the bubble upwards until a terminal velocity is reached. The time at which this terminal velocity is attained depends on bubble volume, but all the bubbles modelled in the super-critical regime will have reached it by $t = 0.3$ s. As can be

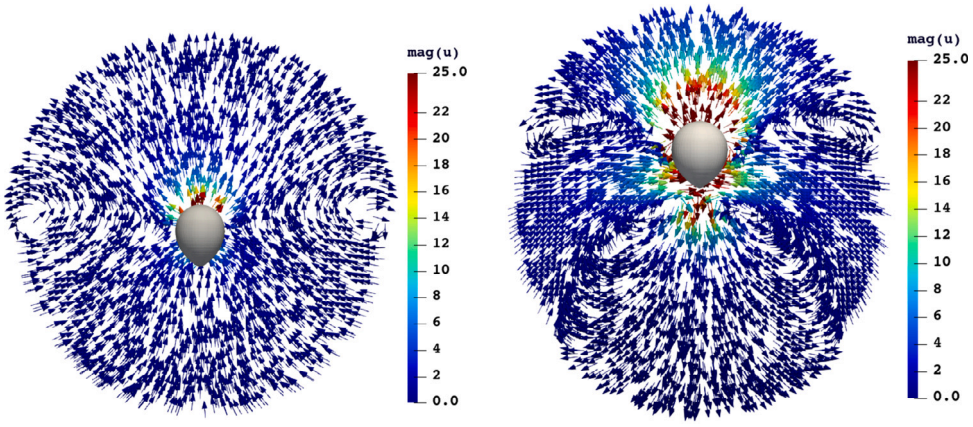

(a) $V = 40\ \mathrm{mm}^3$ (b) $V = 50\ \mathrm{mm}^3$

Fig. 14. Velocity fields for (a) sub- and (b) super-critical bubbles at time $t = 0.3$ s.

seen in Figs. 13a and 13b excellent quantitative agreement is found with the experimental results of Pilz et al. [19] and fully 3D simulations of Bothe et al. [21].

5.2.2. Negative wake

The structure of the velocity field differs greatly between sub- and super-critical bubbles. In Fig. 14 we show the velocity field at time $t = 0.3$ s for bubble volumes $V = 40\ \mathrm{mm}^3$ and $V = 50\ \mathrm{mm}^3$. At this time instance, the sub-critical bubble has long since attained its terminal velocity and the super-critical bubble is just about to reach its value. In Fig. 14a the velocity field is reminiscent of a bubble rising in a Newtonian fluid at low Reynolds numbers. The velocity field is pointing vertically upward with dual vortices either side of bubble. The difference is a small region near the south pole of the bubble in which the velocity field appears to be pointing in the opposite direction. This behaviour is a result of the accumulation of viscoelastic stresses at the cusp of the bubble, however they are not large enough in magnitude to cause the phenomena we observe in Fig. 14b. Here, there are three distinct regions of flow visible. The upward region of flow in front of the bubble with dual vortices is roughly the same as the sub-critical case. Directly beneath the south pole of the bubble exists a large conical region of flow, in which the flow is in the opposite direction to the motion of the bubble and is known as the negative wake. Lastly, there is another set of vortices which are fed by the negative wake and result in fluid flowing into the interface of the bubble below the equator. This behaviour has been predicted experimentally and numerically, which makes it a good physical mechanism to confirm the validity of a numerical scheme.

The negative wake phenomenon has also been observed in solid spheres settling in viscoelastic fluids [41] which indicates that the deformation of the interface as the bubble rises is not a factor that initiates this behaviour in the velocity field. This means there is a complex synergistic effect between elasticity and viscosity which causes the polymer chains to take longer to relax and form a negative wake, for a larger bubble. The negative wake is also present for the sub-critical bubble but disappears as soon as it forms. In contrast the wake stays present for the remainder of simulation time for the super-critical case, indicating that the polymer chains never fully relax in the wake region. This is a specific observable hydrodynamic distinction between sub- and super-critical bubbles, indicating that the negative wake could be used to predict the jump discontinuity.

5.2.3. Normal stress fields

Surface plots of the normal polymeric stress components are shown in Figs. 15 and 16 respectively, together with grey isosurfaces of the bubble interface. We investigate how these fields vary between sub- and super-critical bubbles and for different time instances. The first time instance chosen is $t = 0.06$ s which corresponds to the local minimum in the rise velocity. This is when viscoelastic stresses have built up and the fluid is resisting further deformation. The latter is $t = 0.3$ s which corresponds to when all bubbles have reached their terminal velocity. In Fig. 15 the polymeric stress fields do not vary much between the sub- and super-critical volumes. The distribution of large volumes of τ_{rr} is localised to the north pole, with smaller regions becoming more recognisable either side of the south pole. For τ_{zz} the reverse is true with a region of large stress just beneath the south pole and smaller stress profiles either side of the north pole. This indicates the accumulation of viscoelastic stress at the south pole of the bubble leading to the formation of a cusp and the negative wake. Finally, for $\tau_{\theta\theta}$ the distributions remain almost identical apart from an increase in magnitude and larger distribution of stress further down the interface for the super-critical case.

As time progresses the super-critical bubble experiences a large jump in rise velocity as the negative wake fully forms and the jump discontinuity phenomenon is exhibited. The butterfly-like distribution exhibited by τ_{rr} extends down into the wake in Fig. 16d and can be observed to a lesser degree in Fig. 15d for the sub-critical case. Due to the presence of the negative wake in the super-critical case, the region of negative values of this normal stress component extends much further into the wake in Fig. 16d. The region of large radial stress on the top of the bubble extends over more of the surface in both cases and is of much larger magnitude at the north pole in the super-critical case. The region of large axial normal stress just beneath the bubble becomes longer and

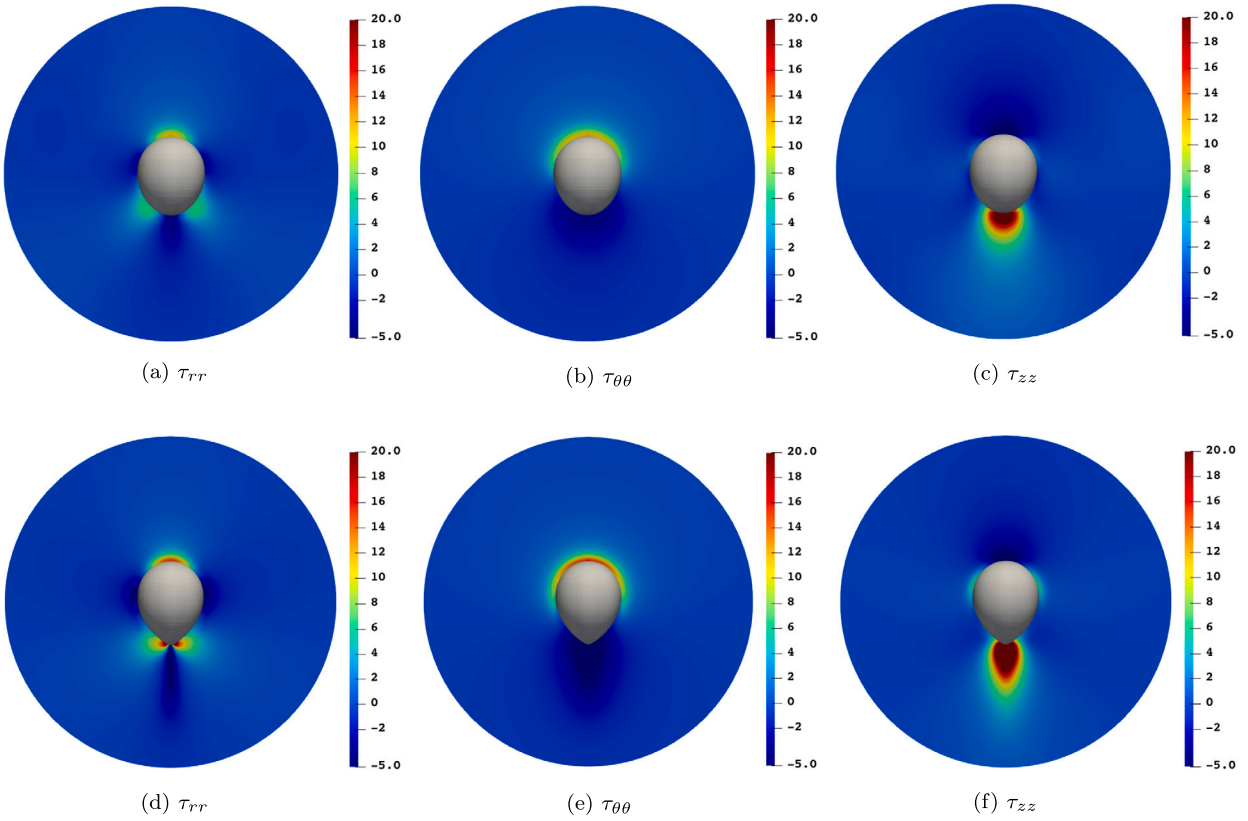

Fig. 15. Polymeric stress contour fields for the normal components of $\boldsymbol{\tau}$ of a sub-critical bubble of volume $V = 40$ mm^3. Figures a) - c) are at time $t = 0.06$ s (local minimum velocity) while Figures d) - f) are at time $t = 0.3$ s (terminal velocity).

thinner between Fig. 15c and Fig. 15f. This is due to the negative wake forming during the first snapshot and then relaxing for the remaining duration of the bubble rise. For the super-critical case, we can see the region of large stress extends much further into the wake in Fig. 16f compared to 16c. This indicates for both cases that the polymers are at their most extended state at $t = 0.06$ s but the difference between sub- and super-critical bubble volumes is that the polymers stay in a more extended state for the latter case. The stress in the circumferential direction $\tau_{\theta\theta}$ depicted in Figs. 15e and 16e has significant differences compared to before. While at $t = 0.06$ s the stress looked very similar between the cases, here the super-critical stress is of much larger magnitude and the region of large stress extends much further around the bubble surface towards the south pole. This stretching of polymers in the circumferential direction and subsequent relaxation is what some papers in the literature cite as one of the main mechanisms in the velocity jump phenomenon [21]. Depending on the rate of transport of polymer molecules along the bubble surface, the hoop stress can generate a force either with or against the direction of rise. The theory of kinematic orientation and stretching is described by Bothe et al. [21] but to summarise, the faster the hoop stress relaxes, the greater the force that resists the rise of the bubble. This means that, as shown in Fig. 15e, the hoop stress deforms and relaxes quickly above the equator of the bubble, and therefore a jump is not exhibited. However as can be seen in Fig. 16e, the relaxation takes place further around the interface, south of the equator and generates an upward force which contributes to the velocity jump. It is also likely that the cusp is also formed by this mechanism, due to the high degree of stretching in the direction of the axis of symmetry just above where the cusp becomes very visible.

6. Conclusions

A mathematical framework and computational model has been presented for axisymmetric single- and multi-phase flows of Newtonian and viscoelastic fluids. In the case of viscoelastic fluids the constitutive equation is expressed in an alternative log-conformation formulation which extends considerably the range of Weissenberg numbers for which numerical solutions are obtained. A novel version of the conservative level-set method is implemented for multi-phase flows in which a diffused normal calculation is used to enhance stability. These numerical techniques are combined within a robust finite element formulation, implemented in the open source finite element library FEniCS [33].

The single-phase axisymmetric viscoelastic model has been validated for the benchmark problem of flow past a sphere in a channel. The Oldroyd B and Giesekus models are considered, the latter for a range of mobility factors. We identify different behaviour in the low Weissenberg number limit (0.1 - 1) and the high limit (2 - 100). The normal axial polymeric stress is largest on the surface of the sphere in the low limit but in the high limit there is more elastic deformation observed in the wake. This value of the polymeric

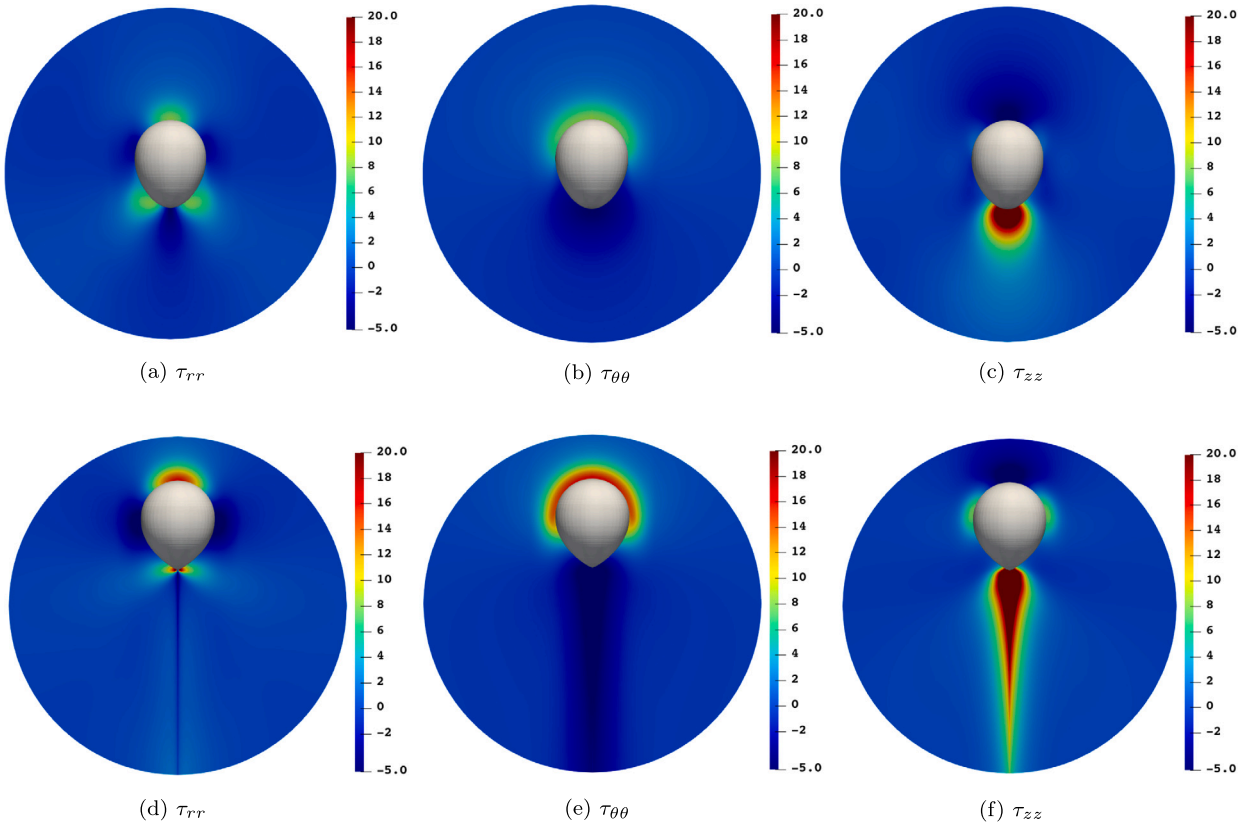

Fig. 16. Polymeric stress contour fields for the normal components of $\boldsymbol{\tau}$ of a super-critical bubble of volume $V = 50$ mm^3. Figures a) - c) are at time $t = 0.06$ s (local minimum velocity) while Figures d) - f) are at time $t = 0.3$ s (terminal velocity).

stress tensor monotonically decreases on the surface of the sphere for high Wi, indicating a relaxation of the polymers with increasing Wi. Excellent agreement with the literature is found for the calculated values of the drag correction factor. Following the contribution of Claus et al. [25] on the energy stability criterion associated with pressure contours, we show that the increasing distortion of the pressure along $z = 0$ leads to an increase in the magnitude of the criterion I until there is a velocity inflection. For the first time we show that this behaviour is present for Giesekus fluids with low mobility factors in an axisymmetric framework. However, as α increases the computations become more stable and the pressure profiles become less distorted with no velocity inflection present.

The multi-phase axisymmetric model is used to study the benchmark problem of a rising bubble in both Newtonian and viscoelastic fluids. Excellent quantitative agreement is achieved with the experimental data of Hnat and Buckmaster [32] for the rise velocity of a bubble in a Newtonian fluid and qualitative agreement is obtained for bubble shapes. The viscoelastic fluid 0.8 wt.% Praestol 2500 is used as the basis for comparisons between numerical predictions and experimental measurements of the bubble rise velocity. Excellent quantitative agreement is achieved in determining the critical bubble volume at which a jump in bubble rise velocity occurs. The structure of the negative wake in super-critical bubbles is investigated and the influence of the normal stresses in generating the jump discontinuity is explored.

The axisymmetric model proposed in this paper is applicable to a wide range of problems in the field of multiphase computational fluid dynamics. For example, it could be used to model the extrusion of a viscoelastic jet and the formation of beads and satellite droplets [12]. In future work we would like to extend our model with the recent development of filament capturing method [42] and also to account for fully 3D dynamics and to compare predictions with the axisymmetric model and experiments. This will allow us to investigate the extent of the range of validity of the axisymmetric assumption and also to study complex 3D multiphase flow problems.

CRediT authorship contribution statement

William Doherty: Data curation, Formal analysis, Investigation, Methodology, Software, Validation, Visualization, Writing – original draft. **Timothy N. Phillips:** Conceptualization, Investigation, Methodology, Writing – review & editing, Supervision. **Zhihua Xie:** Conceptualization, Funding acquisition, Investigation, Methodology, Supervision, Writing – review & editing.

Declaration of competing interest

The authors declare that they have no known competing financial interests or personal relationships that could have appeared to influence the work reported in this paper.

Data availability

Data will be made available on request.

Acknowledgements

The first author would like to thank the United Kingdom Engineering and Physical Sciences Research Council (EPSRC) for providing the funding to support his doctoral study (Grant No. EP/R513003/1 with Studentship reference 2397637). Z.X. was financially supported by EPSRC grant (EP/V040235/1), the Royal Society Newton Advanced Fellowship (NAF/R1/ 201156) and International Exchanges Award (IEC/NSFC/211143, IES/R2/ 202095). This research was undertaken using the supercomputing facilities at Cardiff University operated by Advanced Research Computing at Cardiff (ARCCA) on behalf of the Cardiff Supercomputing Facility and the HPC Wales and Supercomputing Wales (SCW) projects. We acknowledge the support of the latter, which is part-funded by the European Regional Development Fund (ERDF) via the Welsh Government.

Appendix A. Governing equations in cylindrical polar coordinates for axisymmetric viscoelastic flow

Velocity gradient tensor

$$\nabla \mathbf{u} = \begin{bmatrix} \frac{\partial u_r}{\partial r} & \frac{\partial u_r}{\partial z} & 0 \\ \frac{\partial u_z}{\partial r} & \frac{\partial u_z}{\partial z} & 0 \\ 0 & 0 & \frac{u_r}{r} \end{bmatrix} \tag{A.1}$$

Rate-of-strain tensor

$$\mathbf{D}(\mathbf{u}) = \frac{1}{2}\left(\nabla \mathbf{u} + \nabla \mathbf{u}^T\right) = \begin{bmatrix} \frac{\partial u_r}{\partial r} & \frac{1}{2}\left(\frac{\partial u_r}{\partial z} + \frac{\partial u_z}{\partial r}\right) & 0 \\ \frac{1}{2}\left(\frac{\partial u_r}{\partial z} + \frac{\partial u_z}{\partial r}\right) & \frac{\partial u_z}{\partial z} & 0 \\ 0 & 0 & \frac{u_r}{r} \end{bmatrix} \tag{A.2}$$

Continuity equation

$$\frac{1}{r}\frac{\partial (r u_r)}{\partial r} + \frac{\partial u_z}{\partial z} = 0 \tag{A.3}$$

Conservation of momentum

$$\begin{aligned} \rho\left(\frac{\partial u_r}{\partial t} + u_r\frac{\partial u_r}{\partial r} + u_z\frac{\partial u_r}{\partial z}\right) = &-\frac{1}{r}\frac{\partial p}{\partial r} + \eta_s\left(\frac{1}{r}\frac{\partial}{\partial r}\left(r\frac{\partial u_r}{\partial r}\right) + \frac{\partial^2 u_r}{\partial z^2} - \frac{u_r}{r^2}\right) \\ &+ \frac{1}{r}\frac{\partial}{\partial r}\left(r\tau_{rr}\right) + \frac{\partial \tau_{rz}}{\partial z} - \frac{\tau_{\theta\theta}}{r} \\ &- \sigma\left(\frac{1}{r}\frac{\partial (r n_r)}{\partial r} + \frac{\partial n_z}{\partial z}\right)\frac{\partial \phi}{\partial r} \end{aligned} \tag{A.4}$$

$$\begin{aligned} \rho\left(\frac{\partial u_z}{\partial t} + u_r\frac{\partial u_z}{\partial r} + u_z\frac{\partial u_z}{\partial z}\right) = &-\frac{1}{r}\frac{\partial p}{\partial z} + \eta_s\left(\frac{1}{r}\frac{\partial}{\partial r}\left(r\frac{\partial u_z}{\partial r}\right) + \frac{\partial^2 u_z}{\partial z^2}\right) \\ &+ \frac{1}{r}\frac{\partial}{\partial r}\left(r\tau_{rz}\right) + \frac{\partial \tau_{zz}}{\partial z} \\ &- \rho g - \sigma\left(\frac{1}{r}\frac{\partial (r n_r)}{\partial r} + \frac{\partial n_z}{\partial z}\right)\frac{\partial \phi}{\partial z} \end{aligned} \tag{A.5}$$

Constitutive equation - log-conformation formulation

$$\frac{\partial \psi_{rr}}{\partial t} + u_r\frac{\partial \psi_{rr}}{\partial r} + u_z\frac{\partial \psi_{rr}}{\partial z} - 2B_{rr} = -\frac{1 - e^{-\lambda_1}}{\lambda} f(e^{\Psi}) \tag{A.6}$$

$$\frac{\partial \psi_{\theta\theta}}{\partial t} + u_r\frac{\partial \psi_{\theta\theta}}{\partial r} + u_z\frac{\partial \psi_{\theta\theta}}{\partial z} - 2B_{\theta\theta} = -\frac{1 - e^{-\lambda_3}}{\lambda} f(e^{\Psi}) \tag{A.7}$$

$$\frac{\partial \psi_{zz}}{\partial t} + u_r\frac{\partial \psi_{zz}}{\partial r} + u_z\frac{\partial \psi_{zz}}{\partial z} - 2B_{zz} = -\frac{1 - e^{-\lambda_2}}{\lambda} f(e^{\Psi}) \tag{A.8}$$

$$\frac{\partial \psi_{rz}}{\partial t} + u_r \frac{\partial \psi_{rz}}{\partial r} + u_z \frac{\partial \psi_{rz}}{\partial z} - \Omega_{rz}\left(\psi_{zz} - \psi_{rr}\right) = 0 \tag{A.9}$$

Level set equation - advection

$$\frac{\partial \phi}{\partial t} + u_r \frac{\partial \phi}{\partial r} + u_z \frac{\partial \phi}{\partial z} = 0 \tag{A.10}$$

Level set equation - reinitialisation

$$\frac{\partial \phi}{\partial \tau_1} + \frac{1}{r}\frac{\partial}{\partial r}\left(\left[\phi(1-\phi)\mathbf{n}\right)\right]_r + \frac{\partial}{\partial z}\left(\left[\phi(1-\phi)\mathbf{n}\right)\right]_z = \epsilon\left(\frac{1}{r}\frac{\partial}{\partial r}\left(r\frac{\partial \phi}{\partial r}\right) + \frac{\partial^2 \phi}{\partial z^2}\right) \tag{A.11}$$

Level set equation - diffusion

$$\frac{\partial \phi_D}{\partial \tau_2} = D\left(\frac{1}{r}\frac{\partial}{\partial r}\left(r\frac{\partial \phi_D}{\partial r}\right) + \frac{\partial^2 \phi_D}{\partial z^2}\right) \tag{A.12}$$

References

[1] E. Vachagina, N. Dushin, E. Kutuzova, A. Kadyirov, Exact solution for viscoelastic flow in pipe and experimental validation, Polymers 14 (2) (2022) 334, https://doi.org/10.3390/polym14020334.

[2] E. Soto, C. Goujon, R. Zenit, O. Manero, A study of velocity discontinuity for single air bubbles rising in an associative polymer, Phys. Fluids 18 (12) (2006) 121510, https://doi.org/10.1063/1.2397011.

[3] R.G. Owens, T.N. Phillips, Computational Rheology, World Scientific, 2002.

[4] R. Keunings, On the high Weissenberg number problem, J. Non-Newton. Fluid Mech. 20 (1986) 209–226, https://doi.org/10.1016/0377-0257(86)80022-2.

[5] G.H. McKinley, W.P. Raiford, R.A. Brown, R.C. Armstrong, Nonlinear dynamics of viscoelastic flow in axisymmetric abrupt contractions, J. Fluid Mech. 223 (1) (1991) 411, https://doi.org/10.1017/s0022112091001489.

[6] R.G. Larson, Viscoelastic inertial flow driven by an axisymmetric accelerated surface, J. Fluid Mech. 196 (1988) 449–465, https://doi.org/10.1017/s0022112088002770.

[7] W. Doherty, T.N. Phillips, Z. Xie, A stabilised finite element framework for viscoelastic multiphase flows using a conservative level-set method, J. Comput. Phys. 477 (2023) 111936, https://doi.org/10.1016/j.jcp.2023.111936.

[8] K. Walters, R.I. Tanner, The motion of a sphere through an elastic fluid, in: Transport Processes in Bubbles, Drops and Particles, 1992, pp. 73–86.

[9] S. Faroughi, C. Fernandes, J.M. Nóbrega, G. McKinley, A closure model for the drag coefficient of a sphere translating in a viscoelastic fluid, J. Non-Newton. Fluid Mech. 277 (2020) 104218, https://doi.org/10.1016/j.jnnfm.2019.104218.

[10] H.-S. Dou, N. Phan-Thien, Viscoelastic flow past a confined cylinder: instability and velocity inflection, Chem. Eng. Sci. 62 (15) (2007) 3909–3929, https://doi.org/10.1016/j.ces.2007.03.040.

[11] E. Turkoz, H.A. Stone, C.B. Arnold, L. Deike, Simulation of impulsively induced viscoelastic jets using the Oldroyd-B model, J. Fluid Mech. 911 (jan 2021), https://doi.org/10.1017/jfm.2020.1053.

[12] K. Zinelis, T. Abadie, G.H. McKinley, O.K. Matar, Transition to elasto-capillary thinning dynamics in viscoelastic jets, https://doi.org/10.48550/ARXIV.2306.05137, 2023.

[13] M. Rubio, S. Sadek, E.J. Vega, A.M. Gañán-Calvo, J.M. Montanero, Electrical conductivity of a stretching viscoelastic filament, Materials 14 (5) (2021) 1294, https://doi.org/10.3390/ma14051294.

[14] E. Castillo, J. Baiges, R. Codina, Approximation of the two-fluid flow problem for viscoelastic fluids using the level set method and pressure enriched finite element shape functions, J. Non-Newton. Fluid Mech. 225 (2015) 37–53, https://doi.org/10.1016/j.jnnfm.2015.09.004.

[15] A. Amani, N. Balcázar, A. Naseri, J. Rigola, A numerical approach for non-Newtonian two-phase flows using a conservative level-set method, Chem. Eng. J. 385 (2020) 123896, https://doi.org/10.1016/j.cej.2019.123896.

[16] G. Astarita, G. Apuzzo, Motion of gas bubbles in non-Newtonian liquids, AIChE J. 11 (5) (1965) 815–820, https://doi.org/10.1002/aic.690110514.

[17] P.G. Saffman, On the rise of small air bubbles in water, J. Fluid Mech. 1 (3) (1956) 249–275, https://doi.org/10.1017/s0022112056000159.

[18] A.W. Liu, D.E. Bornside, R.C. Armstrong, R.A. Brown, Viscoelastic flow of polymer solutions around a periodic, linear array of cylinders: comparisons of predictions for microstructure and flow fields, J. Non-Newton. Fluid Mech. 77 (3) (1998) 153–190, https://doi.org/10.1016/s0377-0257(97)00067-0.

[19] C. Pilz, G. Brenn, On the critical bubble volume at the rise velocity jump discontinuity in viscoelastic liquids, J. Non-Newton. Fluid Mech. 145 (2–3) (2007) 124–138, https://doi.org/10.1016/j.jnnfm.2007.05.015.

[20] J.R. Vélez-Cordero, D. Sámano, R. Zenit, Study of the properties of bubbly flows in Boger-type fluids, J. Non-Newton. Fluid Mech. 175–176 (2012) 1–9, https://doi.org/10.1016/j.jnnfm.2012.03.008.

[21] D. Bothe, M. Niethammer, C. Pilz, G. Brenn, On the molecular mechanism behind the bubble rise velocity jump discontinuity in viscoelastic liquids, J. Non-Newton. Fluid Mech. 302 (2022) 104748, https://doi.org/10.1016/j.jnnfm.2022.104748.

[22] R. Kynch, T. Phillips, A high resolution spectral element approximation of viscoelastic flows in axisymmetric geometries using a DEVSS-g/DG formulation, J. Non-Newton. Fluid Mech. 240 (2017) 15–33, https://doi.org/10.1016/j.jnnfm.2016.12.008.

[23] J. Venkatesan, S. Ganesan, Local projection stabilized finite element modeling of viscoelastic two-phase flows, https://doi.org/10.48550/ARXIV.1902.06466, 2019.

[24] M.R. Rezaie, M. Norouzi, M.H. Kayhani, S.M. Taghavi, M. Kim, K.C. Kim, On viscoelastic drop impact onto thin films: axisymmetric simulations and experimental analysis, Sci. Rep. 13 (1) (jul 2023), https://doi.org/10.1038/s41598-023-38235-1.

[25] S. Claus, T.N. Phillips, Viscoelastic flow around a confined cylinder using spectral/hp element methods, J. Non-Newton. Fluid Mech. 200 (2013) 131–146, https://doi.org/10.1016/j.jnnfm.2013.03.004.

[26] P. Knechtges, The fully-implicit log-conformation formulation and its application to three-dimensional flows, J. Non-Newton. Fluid Mech. 223 (2015) 209–220, https://doi.org/10.1016/j.jnnfm.2015.07.004.

[27] R. Fattal, R. Kupferman, Constitutive laws for the matrix-logarithm of the conformation tensor, J. Non-Newton. Fluid Mech. 123 (2–3) (2004) 281–285, https://doi.org/10.1016/j.jnnfm.2004.08.008.

[28] E. Olsson, G. Kreiss, A conservative level set method for two phase flow, J. Comput. Phys. 210 (1) (2005) 225–246, https://doi.org/10.1016/j.jcp.2005.04.007.

[29] S. Osher, J.A. Sethian, Fronts propagating with curvature-dependent speed: algorithms based on Hamilton-Jacobi formulations, J. Comput. Phys. 79 (1) (1988) 12–49, https://doi.org/10.1016/0021-9991(88)90002-2.

[30] J.U. Brackbill, D.B. Kothe, C. Zemach, A continuum method for modeling surface tension, J. Comput. Phys. 100 (2) (1992) 335–354, https://doi.org/10.1016/0021-9991(92)90240-y.

[31] Z. Xie, D. Pavlidis, P. Salinas, J.R. Percival, C.C. Pain, O.K. Matar, A balanced-force control volume finite element method for interfacial flows with surface tension using adaptive anisotropic unstructured meshes, Comput. Fluids 138 (2016) 38–50, https://doi.org/10.1016/j.compfluid.2016.08.005.
[32] J.G. Hnat, J.D. Buckmaster, Spherical cap bubbles and skirt formation, Phys. Fluids 19 (2) (1976) 182, https://doi.org/10.1063/1.861445.
[33] M. Alnæs, J. Blechta, J. Hake, A. Johansson, B. Kehlet, A. Logg, C. Richardson, J. Ring, M.E. Rognes, G.N. Wells, The FEniCS project version 1.5, Arch. Numer. Softw. 3 (2015), https://doi.org/10.11588/ANS.2015.100.20553.
[34] A.N. Brooks, T.J.R. Hughes, Streamline upwind/Petrov-Galerkin formulations for convection dominated flows with particular emphasis on the incompressible Navier-Stokes equations, Comput. Methods Appl. Mech. Eng. 32 (1–3) (1982) 199–259, https://doi.org/10.1016/0045-7825(82)90071-8.
[35] J. Marchal, M. Crochet, A new mixed finite element for calculating viscoelastic flow, J. Non-Newton. Fluid Mech. 26 (1) (1987) 77–114, https://doi.org/10.1016/0377-0257(87)85048-6.
[36] R.G. Owens, C. Chauvière, T.N. Philips, A locally-upwinded spectral technique (LUST) for viscoelastic flows, J. Non-Newton. Fluid Mech. 108 (1–3) (2002) 49–71, https://doi.org/10.1016/s0377-0257(02)00124-6.
[37] D. Gueyffier, J. Li, A. Nadim, R. Scardovelli, S. Zaleski, Volume-of-fluid interface tracking with smoothed surface stress methods for three-dimensional flows, J. Comput. Phys. 152 (2) (1999) 423–456, https://doi.org/10.1006/jcph.1998.6168.
[38] K. Yokoi, A practical numerical framework for free surface flows based on CLSVOF method, multi-moment methods and density-scaled CSF model: numerical simulations of droplet splashing, J. Comput. Phys. 232 (1) (2013) 252–271, https://doi.org/10.1016/j.jcp.2012.08.034.
[39] W. Yuan, M. Zhang, B.C. Khoo, N. Phan-Thien, On peculiar behaviours at critical volumes of a three-dimensional bubble rising in viscoelastic fluids, J. Non-Newton. Fluid Mech. 293 (2021) 104568, https://doi.org/10.1016/j.jnnfm.2021.104568.
[40] M. Niethammer, G. Brenn, H. Marschall, D. Bothe, An extended volume of fluid method and its application to single bubbles rising in a viscoelastic liquid, J. Comput. Phys. 387 (2019) 326–355, https://doi.org/10.1016/j.jcp.2019.02.021.
[41] C. Bisgaard, Velocity fields around spheres and bubbles investigated by laser-Doppler anemometry, J. Non-Newton. Fluid Mech. 12 (3) (1983) 283–302, https://doi.org/10.1016/0377-0257(83)85003-4.
[42] P. Hergibo, T.N. Phillips, Z. Xie, A moment-of-fluid method for resolving filamentary structures using a symmetric multi-material approach, J. Comput. Phys. 491 (2023) 112401, https://doi.org/10.1016/j.jcp.2023.112401.